Final Report of Research Project

of

National Science Council

Kuroshio Intrusion in Luzon Strait

黑潮於呂宋海峽的入侵

By
T. Y. Tang
唐存勇

Institute of Oceanography
National Taiwan University
Taipei, Taiwan, ROC

Research Project No: NSC 89-2611-M-002-031-OP2

May 2002

1. 簡介

在計畫書中承諾以蒐集的海洋資料配合數值式研究探討黑潮於呂宋海峽的入侵及其在北南海的行為。研究執行尚稱亦好，撰寫一篇論文 – Kuroshio Intrusion in Luzon Strait，目前已送至 Journal of Physical Oceanography 審查，二審查人皆建議接受但須要一定程度的修改。另外亦完成一篇有關黑潮與北南流的作用結果，文章名為 “ Intra-seasonal variation in the velocity field of the northeastern South China Sea ”，文章已運 Geophysical Research Letter 審查中。計畫主持人另有數篇 papers，或已接發表，或正在 in press，或仍在審查修正中，但因這些 papers 與此計畫無直接關連，故未列入此報告中。

第 2 章將二篇論文陳列做為此計畫的成果，第 3 章將討論結果的缺失，及未來可能進一步研究之方向

2. 結果

Kuroshio Intrusion in the Luzon Strait

By

T. Y. TANG[1], W.-D LIANG[2], Y. J. YANG[3], and W.-S. CHUANG[1]

[1]*Institute of Oceanography, National Taiwan University, Taipei, Taiwan, ROC*
[2]*National Center for Ocean Research, Taipei, Taiwan, ROC*
[3]*Department of Marine Science, Chinese Naval Academy, Tsoying, Kaohsiung, Taiwan, ROC*

Submitted to Journal of Physical Oceanography

October 2002

ABSTRACT

Three Acoustic Doppler Current Profilers (ADCP) were deployed in the central Luzon Strait to monitor current velocity. The duration of deployment varied with location and spanned from 1997 to 1999. The observed current velocity indicated that the Kuroshio consistently intruded into the South China Sea. The current velocity demonstrated small annual variation, but large intraseasonal variation. The change of monsoons, from northeast to southwest, did not cause noticeable variation in current velocity.

The Miami Isopycnic Coordinate Ocean Model (MICOM) forced by the wind data provided by the European Centre for Medium-Range Weather Forecasts (ECMWF) was used to interpret the observed current velocity. Comparison between the model output and observation validates the use of the model result in interpreting annual and interannual current velocity variation in the Luzon Strait. The numerical model result also shows that the Kuroshio consistently intruded into the South China Sea, displaying a noticeable annual variation in the central Luzon Strait. The large interannual variation masked the annual variation so that the annual variation was difficult to observe. The interaction between the Kuroshio and the South China Sea cyclonic flow caused the current velocity variation in the both the Luzon Strait and the northern sector of the South China Sea. In summer, the Kuroshio intrudes as a

loop current intrusion and confines to the northern South China Sea. In winter, the Kuroshio can intrude deeply into the South China Sea, besides intruding as loop current intrusion in the northern South China Sea.

The annual transport variation across the Luzon Strait is primarily westward. The eastward transport was found in summer during certain years when the Kuroshio intrusion was weak. In spite of the fact that the Kuroshio intruded consistently into the South China Sea, transport out of the South China Sea was observed. In summer, the current on the northern South China Sea shelf break contributed to the transport out. The variation in zonal transport was caused by the Sea Surface Height (SSH) variation occurring west of northern Luzon. Wind stress curl is responsible for this SSH variation. The variation of Kuroshio strength had little impact on the intrusion.

1. Introduction

The Luzon Strait is located between Taiwan and Luzon. It is the primary channel for exchanging water between the South China Sea and the North Pacific Ocean. The width of the Luzon Strait, from southern Taiwan to northern Luzon, is around 350 km. It is shallow at both the northern and southern ends and is deep in the central portion. The maximum water depth is over 2500 m. The topography is generally complicated in and around the Strait. A number of small islands are located at the southern end of the Luzon Strait. The water depth increases rapidly to the east and west of the Strait, where it meets the basins of the northern Pacific and South China Sea. A shelf break occurs northwest of the Luzon Strait, where the Taiwan Strait joins the South China Sea and the East China Sea. The current in the Luzon Strait might affect the flow in the Taiwan Strait and possibly even the East China Sea.

The Luzon Strait is the first large meridional gap for the principal North Pacific Western Boundary Current (the Kuroshio). Whether the northward Kuroshio leaps across the Luzon Strait or intrudes into the South China Sea through the Luzon Strait is an issue that has often drawn oceanographers' attention. Wyrtki (1961) and Nitani (1972) suggested that the Kuroshio intruded into the South China Sea when the northeast monsoon prevailed, halting when the southwest monsoon was dominant.

This seasonal intrusion feature was re-confirmed by many scientists. Levitus (1982) studied the Volunteer Observing Ship data (VOS); Shaw (1991) analyzed historical hydrographic measurements, and Farris and Wimbush (1996) examined satellite-derived Sea Surface Temperature (SST) images. All reached a similar conclusion; Kuroshio intrusion occurs seasonally. Shaw and Chao (1994) forced a numerical model based on the monthly climatological wind and also re-produced the above findings. Nevertheless, a few studies obtained different results. For example, Chu (2000) used the climatological hydrographic data to estimate intruded Kuroshio transport in the Luzon Strait. The transport varied seasonally, but was consistently westward, with the largest amount 13.7 Sv in February and the smallest amount 1.4 Sv in September. Using the historical temperature profiles, Qu (2000) obtained similar results; the transport was westward consistently, but with different estimated amounts of transport. The largest intruded volume was 5.3 Sv in January through February and the smallest intruded volume was 0.2 Sv in June through July. The numerical model produced by Metzger and Hurlburt (1996) displayed the features stated in the findings of Qu (2000).

The mechanisms causing Kuroshio intrusion have also been a subject of controversy. Stommel and Arons (1960) claimed that the western boundary current always intruded as it encountered a meridional gap due to the beta effect. Sheremet

(2001) indicated that the western boundary current could leap across the meridional gap when the gap is small or the inertia is large. He inferred that the Kuroshio intruded into the South China Sea in the season of northeast monsoon because the speed of the Kuroshio was weakened by the head wind. Analyzing the hydrographic measurements, Wang and Chern (1987) postulated that the Ekman transport, induced by the monsoon, could be important for Kuroshio intrusion. The current in the South China Sea could also be a factor affecting Kuroshio intrusion (Shaw and Chao, 1994). Qu (2000) and Metzger and Hurlburt (1996) concluded that Kuroshio intrusion in the Luzon Strait was primarily related to the meridional pressure gradient across the Strait. All of these controversies are primarily the result of insufficient data, especially in long-term moored current velocity measurements.

Liang et al. (2002) presented a composite current velocity, which was obtained from 10 years of Ship-board Acoustic Doppler Current Velocity Profilers (Sb-ADCP), positioned around Taiwan. The data revealed that the Kuroshio intruded into the South China Sea through the central Luzon Strait. The volume transport in the upper 300 m water column across the Strait was 3.3 Sv westwardly. The intruded Kuroshio interacted with the current in the South China Sea, forming a complicated spatial distribution west of the Luzon Strait. Liang et al. (2002) produced a few moored current velocity time series around the Luzon Strait, which indicated that the

Kuroshio intrusion might be constant. Similar, but more complete moored current velocity measurements are presented in this paper to study Kuroshio intrusion. The moored current velocities are used to examine the validation of outputs of the Miami Isopycnic Coordinate Ocean Model (MICOM; Bleck and Smith 1990; Bleck et al. 1992; Bleck and Chassignet 1994), which was forced by the European Centre for Medium-Range Weather Forecasts [ECMWF (1995)] wind. Using the model outputs, the factors causing Kuroshio intrusion are investigated. Since only monthly wind data was applied, the studies focus on the annual and interannual variations of Kuroshio intrusion in the Luzon Strait. This paper proceeds as follows. In Section 2, the moored current velocity in the Luzon Strait is presented. The Kuroshio intrusion is described. In Section 3, the scheme of the numerical model is stated and the observation and model output comparison is shown. The validation of model outputs is discussed. Section 4 states the annual and interannual evolutions of Kuroshio intrusion. The mechanisms causing such evolutions are examined. A discussion and summary are provided in Section 5.

2. Observation

Figure 1 shows the locations of 3 moorings (named L1, L2, and L3), their surrounding bathymetry, and the composite Sb-ADCP current velocity vectors at 30 m around Taiwan. The asterisk indicates Lanyu Island, where the wind record was used. The moorings were located in the central portion of the Luzon Strait. L1 and L3 were 120 km away from the tips of southern Taiwan and northern Luzon, respectively. L2 is located between them. Moorings were located about 50 km from each other. The water depth at L2 was deepest (over 2000 m), with L1 and L3 depths of around 1300 m and 1650 m, respectively. The composite current velocities, adopted from Liang et al. (2002), indicate that L1 and L2 were located on the main path of Kuroshio intrusion, while L3 was positioned near the southern intrusion boundary. The duration of deployments varied with location. A few refurbishments had to be made during deployment. Table 1 lists the start and ending times, the depth of the instrument position, and local water depths for each deployment. The moorings in the Luzon Strait had a large vertical excursion, especially at L2, where the vertical excursion was occasionally greater than 200 m. The large vertical excursion was primarily caused by the high tidal current speed. The tidal current speed (recorded by VACM current meter and not shown) at 1100 m was nearly 100 cm s^{-1} during spring tide. An attempt was made to increase floatation in order to keep the mooring line upright. The mooring line broke and one mooring was lost. Fortunately, all of the moorings had small pitching and rolling angles. As a result, the moored ADCP transducers remained upright. At L2, the

ADCP was kept at a much shallower depth than the range (around 300 m) of the narrow-band ADCP. The design, in combination with the ADCP range being larger than the monitor range, made it possible to record the upper layer current velocities simultaneous with the depth correction. A SEACAT CTD was mounted immediately beneath the ADCP. It provided pressure data, which was used for the depth correction. Short time gaps occasionally occurred at the uppermost depths and were interpolated linearly. Fluctuations of horizontal speed caused by the vertical excursions were estimated. Assuming that the maximum vertical excursion was 300 m, the ADCP moved horizontally about 1054 m over half of the semidiurnal tidal period (6.21 hours) at a location where water depth was 2000 m. The estimated maximum horizontal speed caused by the vertical excursion was less than 10 cm s^{-1}. It would not significantly bias the large subtidal current velocity in the Luzon Strait.

Figure 2 shows the eastward (*U*) and northward (*V*) components of current velocity at L1, where water depth is 1300 m. The depth (30-220 m) average of *U*, *V*, and their velocity sticks time series are also shown. The time series was low-pass filtered to remove the fluctuations for frequencies higher than 0.0139 cycles per hour (cph). The data covers a period of 1.5 months in 1997 and nearly 12 months beginning April 1998. Westward velocity dominated in *U*. Eastward current was only apparent for short periods of time. The westward current had high speed (maximum around 70 cm s^{-1}) at the surface and gradually decreased with depth (the decreasing rate about 0.6 cm s^{-1} every 10 m). The seasonal change was vague. The transition of monsoons usually occurred in April and September (Chuang and Liang 1994) and had no significant impact on the *U*. Northward current dominated in the *V*. Southward current was rarely observed. The greatest *V* (maximum over 110 cm s^{-1}) occurred at the uppermost depth, decreasing with increasing depth (the decreasing rate about 1.4 cm s^{-1} every 10 m). The *V* at depths below 200 m was generally less than 20 cm s^{-1}. The *V* was weak from December through February when the northeast monsoon gained full strength. The depth-averaged time series showed that the *U* and *V* fluctuated, but their variance spectra (not shown) had no significant peak in the specific frequency band. In general, the *U* had smaller amplitude than *V*. In a peak-to-peak comparison, the north and east component velocities frequently varied out of phase. The velocity sticks showed that the current at L1 moved primarily to the north-northwest, but was more westward as velocity stick amplitude decreased. The impact of typhoon on the current velocity was not clear. For example, the super Typhoon, Zeb (minimum surface pressure of 880 mbar), moved almost exactly along the mooring array in the Luzon Strait from south to north on October 14-16 of 1998. It only induced short-term velocity fluctuations in the upper ocean, and can be barely observed in the present figures.

The low-pass filtered *U* and *V* at L2 are shown in Fig. 3. L2 is near the center of the Luzon Strait where the water is deep (around 2200 m). The ADCP was mounted at depths of 130 and 160 m for the two deployments in 1997, respectively. These depths were shallower than the range of the ADCP. The rationale for keeping the ADCP at shallow depth was explained above. Due to a mistake in mooring line length, the ADCP was deployed at deeper depths in 1998. The range of available current velocity was from 130 to 280 m. Nearly 9 months of current velocity data, obtained in 1997, was used to describe the upper ocean current velocity at L2. The current velocity obtained in 1998 was used as a reference. Like the current at L1, *U* and *V* at L2 were dominated by the westward and northward component velocities, respectively. Eastward and southward component velocities were rarely observed. The maximum speed was around 100 cm s^{-1} for both westward and northward component velocities. The greatest velocity occurred in the uppermost layer, decreasing with depth (the decreasing rate about 1.0 cm s^{-1} every 10 m). The depth-averaged *U* and *V* had similar amplitudes. The current flowed primarily northwest, which was more westward than the current at L1. Peak-to-peak comparison indicated that the variations of *V* and *U* were frequently out of phase. Although the recorded velocity time series was shorter than a year, it covered the periods when the northeast and southwest monsoons were strong. No clear seasonal difference was found. For example, the velocity in January through February, when the northeast monsoon was dominant, showed little difference from the velocity in May through July, when the southwest monsoon prevailed. The variance spectra of *U* and *V* showed no distinctive peak at any specific frequency band. The current fluctuated with various time scales. The velocity sticks indicated that the current usually flowed toward the northwest. The deeper current velocity, measured in 1998, was more northward than the shallower current velocity, measured in 1997. This dissimilarity might be caused by the difference in depth.

Figure 4 shows the low-pass filtered *U* and *V* at L3. The current velocity at L3 had quite different characteristics than it did at L1 and L2. The *U* was weak (maximum speed around 50 cm s^{-1} and decreasing rate about 0.6 cm s^{-1} every 10 m) and changed its sign repeatedly. The *V*, dominated by northward velocity, was also weaker (maximum speed less than 80 cm s^{-1} and decreasing rate about 0.7 cm s^{-1} every 10 m) than it was at the previous two stations. No seasonal preference was observed in either *U* or *V*. For all of the nearly 9-month record, the mean of *U* was near zero, while the mean of *V* was about 11 cm s^{-1} (northward). The depth (30-160 m) averaged current fluctuated with different time scales and different directions. However, the current was northward more often than not.

In combination with the moored current velocity and Sb-ADCP composite current velocity spatial distribution in the Luzon Strait, a conclusion can be drawn. The Kuroshio intruded consistently into the South China Sea through the central Luzon Strait. It had small annual variations. L1 and L2 were located in the main path of the Kuroshio intrusion. L3 appears to be a southern boundary of Kuroshio intrusion where the Kuroshio intrusion was frequently observed to change to South China Sea outflow. Figure 5 shows the T-S diagrams at L1, L2, L3, the South China Sea and the upstream Kuroshio. An average of 5 CTD measurements (marked by asterisk in Fig. 5) west of Luzon represents the South China Sea water. An average of 3 CTD measurements (marked by cross in Fig. 5) northeast of Luzon represents the upstream Kuroshio. The Kuroshio was saltier and warmer than the South China Sea in the upper water column, but was less salty and colder in the lower water column. Two T-S curves intersected at σ_t = 25.66. The T-S curve at L3 was close to the South China Sea, but gradually moved closer to the curve of Kuroshio water as the location moved north. This finding provides extra evidence that L3 could be the southern boundary of the intruded Kuroshio. However, the T-S curves at 3 stations were notably different than T-S curves from the South China Sea and the Kuroshio. This result implies that the Kuroshio and South China Sea water mix vigorously in the Luzon Strait. The intense current could cause the water mixing.

The northeast-southwest (main) component wind velocity at Lanyu Island in

1997 is shown in Fig. 6. The positive/negative wind velocity flows to the northeast/southwest. The depth-average current velocity of *U* and *V* at L2 are also shown. Overall coherences (not shown) between the current and wind velocities were generally low. However, the peak-to-peak comparison shows that the current fluctuation coincided occasionally with wind fluctuation. For example, the large southwesterly wind oscillation in early June corresponded to the variations in both *U* and *V*. Similar features were also found at L1 and L3, indicating that the local wind played a role, but not the only one.

3. Numerical model

a. Model description

The MICOM model was applied in the numerical simulation. It is a primitive equation numerical model that describes the evolution of momentum, mass, heat, and salt in the ocean, configured with realistic topography and stratification. In contrast to the traditional vertical coordinate of water depth in the level model, MICOM uses equations that have a coordinate of density in the vertical direction. The advantage of a layer model using density coordinate is that the system suppresses the diapycnal component of numerically caused dispersion of material and thermodynamic properties. This characteristic allows isopycnal models to avoid the artificial warming of deep-water masses, as has been shown to occur in level model applications (Chassignet et al. 1996).

The model domain includes the western Pacific and the South China Sea with boundaries at 20.8°S, 45.1°N and 95°E, 160°E (Fig. 7). The horizontal grid is defined on a Mercator projection with resolution given by 1/4° × 1/4°cosϕ (meridional × zonal), where ϕ is the latitude. The vertical density structure has 15 isopycnic layers, topped by a Kraus-Turner mixed layer (Kraus and Turner 1967). The topography was interpolated from the ETOPO5 dataset (NOAA 1988). The model is spun up for 10 years from rest; with an initial thermohaline condition interpolated from the 1994 World Ocean Atlas (WOA94) (Levitus and Boyer 1994; Levitus et al. 1994) January temperature and salinity data. The model was forced by the climatological monthly atmospheric momentum, heat and freshwater flux. The momentum flux was calculated from 1985-1999 wind data provided by the ECMWF with the drag coefficient described in Trenberth et al. (1989). The heat flux, evaporation and precipitation were taken from the Comprehensive Ocean-Atmosphere Data Set (COADS) (da Silva et al. 1994). The layer thickness, temperature and salinity were relaxed to the climatology of the WOA94 monthly data in a 4° buffer zone at the borders of model domain. This 10-year spin up model was continuously forced using 1996-2001 ECMWF monthly wind data, while the heat and freshwater flux were still forced by the climatology.

b. Observation and model comparison

Figure 8 shows the comparison between the observation and model output of monthly average current velocity vectors at various depths and locations. The agreement between model output and observation was good at L1, fair at L2, and poor at L3. The two velocities at L1 were almost identical in direction, but the observed current velocity had slightly larger amplitude than the model. At L2, good agreement was also found in the upper 100 m water columns in 1997. The model output velocity was only slightly more westward than the observed velocity. In the lower water column (130-240 m) in 1998, the two current velocities had noticeable differences in direction. The model output velocity was more westward. At L3, the direction difference between the two velocities became more pronounced. The observed current was primarily northward while the model output velocity was principally northwestward. Although the difference between the two velocities at L3 was noteworthy, for both, the speed was smaller than it was at L1 and L2. L3 is close to the margin of Kuroshio intrusion.

The comparison between model output and observed depth-averaged velocity time series at L1, L2, and L3 is shown in Fig. 9. A 5-day convolution average was applied to both observation and model output. In general, the model output and observation agree well in the low frequency variations at L1 and L2. Fluctuations with time scales of several days to months, were large in the observed velocity, but were not found in the model output. This could be related to the fact that the coarse grid and monthly wind were applied to the model. The mean velocities, calculated from model and observation, are nearly the same. Only slight differences were found in V at L1 and U at L2. The annual variation was small for both model and observed velocities. Even with the assistance of model output, such small annual variation was not easily discernible. At L3, the model and observation had good agreement in the low frequency variation of V, but not U. The mean of observed U was nearly zero, while the mean of modeled U was -27 cm s^{-1}. In the model output, the Kuroshio consistently intruded into the South China Sea through L3. This disagreement could be due to the fact that islands in the southern Luzon Strait were not adequately represented in the model.

The above comparison both validates and limits the use of model output. Good agreement in low frequency variation allows us to use the model output to study annual and interannual variations. Conversely, the fact that model output lacks high frequency variations prohibits its use for study of the intraseasonal variation, observed in the Luzon Strait.

c. Model output

The current velocity distributions at 50 m depth in June and December obtained from the 10th year spin up model outputs in the region of 105°-130°E, 5°-25°N are shown in Fig. 10. The Sea Surface Height (SSH) of the model output is also shown. In June, the westward North Equatorial Current (NEC) in the western Pacific was located primarily in the region of 10°-17°N. It separated into the northward Kuroshio and southward Mindanao Current around 13°N as it approached Mindanao. The Kuroshio flowed primarily northward along the eastern coast of the Philippines, bending into the Luzon Strait, after leaving Luzon, but not immediately after. The inertia effect might keep the swift Kuroshio flowing in its original direction when it first leaves its western continental boundary. Meanwhile, the eastward current in the southern Luzon Strait might prevent the Kuroshio from immediately intruding into the South China Sea. The eastward current originates from the central or southwestern South China Sea. A cyclonic flow, with double or tripe low-pressure (low SSH) centers, was observed west of the Luzon Strait. This cyclonic flow varied seasonally. It was weak and primarily confined to the northern South China Sea during the southwest monsoon season, while it was strong and became a basin-wide feature during the season of northeast monsoon. This cyclonic flow is referred to, hereafter, as South China Sea cyclonic flow. In the Luzon Strait, the Kuroshio separates into two branches. One branch curves slightly clockwise and then flows primarily northward and leaps across the Luzon Strait. The other branch intrudes into the South China Sea and gradually merges and then cycles with the South China Sea cyclonic flow. Only a small portion of the Kuroshio spilled over the shelf and entered the Taiwan Strait. The current in the Taiwan Strait primarily originated from the northern South China Sea shelf break or even further south, from the eastern boundary of Vietnam.

The main feature of Kuroshio intrusion in December was similar to that in June, but with some noticeable differences. In December, the region of NEC greatly expanded northward and the origination of the Kuroshio moved slightly northward. The surface current velocity distributions, obtained from the World Ocean Circulation Experiment/Tropical Oceans Global Atmosphere (WOCE/TOGA) drifting buoys (Hansen and Poulain, 1996), also revealed the feature of seasonal expansion/contraction of the NEC in the western Pacific. The westward NEC reached the northern tip of Luzon. The Kuroshio immediately curves to the northwest, as it leaves Luzon. It again separates into two branches in the Luzon Strait. One leaps across the Strait. The other branch intrudes into the South China Sea and gradually merges with the South China Sea cyclonic flow. In the meanwhile this cyclonic flow, included a stronger meso-scale cyclonic flow in northeastern section and a weaker one in the southwest section, is nearly basin-wide. A strong low-SSH appears west of northern Luzon and southern Luzon Strait. The intruded Kuroshio flows primarily with the South China Sea cyclonic flow into the central and southern South China Sea. A small portion of the intruded Kuroshio curves clockwise, flowing along the southern opening of Taiwan Strait. It either enters the Taiwan Strait or flows out through the southern tip of Taiwan added to the Kuroshio. The current on the northern South China Sea shelf break is weaker in December than in June. The Kuroshio becomes an important source for current in the Taiwan Strait in December. It is noteworthy that the meridional gradient of the SSH across the Luzon Strait is larger in December than in June.

In Fig. 10, it is also shown that the Luzon Strait is not the only opening in the South China Sea. Besides, the South China Sea circulation system is mainly driven by the monsoon. It causes that the Kuroshio in the Luzon Strait differs from the loop current of Gulf Stream in the Gulf of Mexico. The cyclonic flow west of the Luzon Strait confined the loop current in the northern South China Sea. And due to the shallow water of the continental shelf southeast of China, the bottom friction causes that the eddy is seldom shedding from the loop current and less than 100 km in length scale. Even the shedding eddy could not be alive for long. Contrary the Kuroshio in the Luzon Strait, the Mindanao Current in the Sulawesi Sea is more similar to the loop current of Gulf Stream in the Gulf of Mexico. The eddy is often shedding from loop current and more than 300 km in length scale. The shedding eddy is moving westwardly and deceasing in the western Sulawesi Sea.

In general, the Kuroshio only intrudes as a loop current intrusion and confines to the northern South China Sea in summer. In winter, the Kuroshio can intrude deeply into east of Vietnam, besides intruding as loop current intrusion in the northern South China Sea.

4. Kuroshio Intrusion

a. Current around the Luzon Strait

Focusing on Kuroshio intrusion, Figure 11 shows the current velocity distributions at 50 m and SSH around the Luzon Strait. The figure contains 20 panels, 5 rows by 4 columns. Four columns, from top to bottom, represent the current velocity on 15th of March, June, September and December, while 5 rows, from left to right, represent years 1997, 1998, 1999, 2000, and 2001. The current velocity distributions in 1997 are used to illustrate the annual evolution. The greatest Kuroshio intrusion into the South China Sea occurred in March. The South China Sea cyclonic flow with strong low SSH center was found immediately west of the southern Luzon Strait. The intruded Kuroshio flowed with the South China Sea cyclonic flow. A small portion of the Kuroshio spilled out, entering the Taiwan Strait. In June, the Kuroshio consistently intruded into the South China Sea and merged with the cyclonic flow. However, when the South China Sea cyclonic flow was weak and shifted to the west, the strength of the Kuroshio in the Luzon Strait weakened, and the current on the northern shelf break of the South China Sea intensified. The westward shift of the South China Sea cyclonic flow opened a space that allowed a portion of intruded Kuroshio to turn clockwise south of the Taiwan Strait. This clockwise flow either entered into the Taiwan Strait or poured back into the Kuroshio. However, the main source of Taiwan Strait current was from the northern South China Sea shelf break. In September, the South China Sea cyclonic flow and low SSH moved further west. West of the Luzon Strait, the flow became complicated. The Kuroshio in the Luzon Strait also weakened, but it still intruded into the South China Sea. A large portion of intruded Kuroshio retroflexed in a clockwise motion, south of the Taiwan Strait, and then partially entered the Strait. Some exited the South China Sea by flowing out through the northern Luzon Strait. In December, the South China Sea cyclonic flow re-intensified itself, and expanded throughout the basin. The speed of the Kuroshio in the Luzon Strait increased, and the amplitude of the current in the northern South China Sea shelf break decreased. An annual cycle was completed. Obviously, the location and strength of South

China Sea cyclonic flow has large impact on the annual variation of Kuroshio intrusion and the flow west of Luzon Strait. Although the pattern of annual evolution was basically repeated in subsequent years, there were some differences. The most visible difference was that the South China Sea cyclonic flow (or low SSH center) was much stronger in 1997 than in 1998, except for December. The weak SSH center regained its strength gradually from 1999-2001. This interannual variation of South China Sea Cyclonic flow caused the variation of Kuroshio intrusion and flow west of Luzon Strait. For example, the low SSH center was greatest and closest to Taiwan in March of 1997. It caused the Kuroshio to intrude more northward, directly impinging on the southern opening of the Taiwan Strait. The small anti-cyclonic flow that was consistently seen south of Taiwan Strait disappeared.

b. Volume Transport across Luzon Strait

Using the model output and taking a slice along 120.75°E from 18.5 to 22°N, the depth-averaged *U* in the upper 300 m water column and SSH as a function of time and latitude, are shown in Fig. 12. The 3 straight lines indicate mooring locations. The distribution of *U* in the Luzon Strait could be separated into 3 parts. The *U* at the northern and southern parts was essentially eastward, flowing out of the South China Sea. It was generally quite stable and the annual and interannual variations were small. The *U* in the central Luzon Strait varied annually as well as interannually. The westward current velocity was high in winter and low in summer. The model result suggests that annual variations at L2 should be obvious, but at L1 and L3, they might be difficult to discern. However, the annual variations could be hidden by the interannual variations. The annual variations, even in the model output, were unclear in 1997 because of the large interannual variations. This might explain why the observations at L2 in 1997 did not reveal annual variations.

Both annual and interannual SSH variation was small in the northern Luzon Strait, and large in the central southern Luzon Strait, with the lowest and highest SSH generally appearing in November-December and July-August, respectively. For the interannual, the SSH appears to have had its lowest value early in 1997, increasing for the subsequent two winters, and finally decreasing again for the next two winters. The lowest SSH had no significant differences between 2000 and 2001. The position of the lowest SSH moved interannually, but only slightly. The development/ contraction of South China Sea cyclonic flow is related to these variations.

Integrating the modeled *U* in the upper 300 m along 120.75°E from 18.5 to 22°N, Figure 13 shows the time series of zonal transport across the Luzon Strait. The negative and positive values represent the westward and eastward transport, respectively. The zonal transport across the Luzon Strait displayed a clear annual variation. The massive westward Kuroshio intrusion occurred from November through December, when the SSH at the central southern Luzon Strait also reached its lowest value. Its maximum amplitude was over -6 Sv. The westward intrusion generally stopped, and even reversed in summer. Eastward transport in summer was not only related to the reduction of Kuroshio, but was also related to the increased flow in the northern South China Sea shelf break. This shelf flow eventually worked its way out of the South China Sea through the northern Luzon Strait. The annual variation of zonal transport in the upper 300 m across the Luzon Strait generally varied from 0.2 to –5.4 Sv. The zonal volume transport also displayed an interannual variation. In 1997, the major westward intrusion was extraordinarily large through late March. No reversed zonal transport was found in the summer. Westward transport developed unusually small amplitude in winter. Large eastward transport observed in the summer of 1998. Since then, the annual evolutions in subsequent years were similar, but the transport gradually increased westwardly. In 2001, the eastward transport was barely seen in summer, and the amount of annual westward transport was close to that of 1997. The amplitude of interannual variation of zonal transport could reach as large as 3 Sv. The El Niño occurred in 1997 (Boulanger and Menkes 1999; McPhaden 1999; McPhaden and Yu 1999; Kutsuwada et al. 2002) and was predicted to occur in 2002 (CPC/NCEP 2002). Apparently, the interannual variation of zonal transport across the Luzon Strait may have a cycle with El Niño.

To explore the mechanism causing the variation of zonal transport across the Luzon Strait, the zonal Ekman transport across the Luzon Strait was calculated first using the ECMWF wind stress. Figure 14 shows the principle component (northeast-southwest) of ECMWF wind stress at the center of the Luzon Strait and zonal Ekman transport across the Luzon Strait. The wind stress varied annually, as well as interannually. The northeast monsoon, prevalent from September through April, displayed larger amplitude than the southwest monsoon, which was dominant from May through August. The monsoon was weaker starting in the late El Niño Year (1997) and remained weak for about one year. These variations have been described in detail by several oceanographers, including, Chao and Shaw (1996), Liang et al. (2000), etc. The zonal Ekman transport, calculated directly from the wind stress, also varied annually as well as interannually. It had good correlation with the total zonal transport, but its amplitude was much smaller. The contribution of Ekman transport to the total zonal transport was generally less than 15%, which is close to the estimate of Qu (2000). Obviously, some other mechanism is important for causing the zonal transport variation across the Luzon Strait.

Figure 15 shows the SSH west of the southern tip of Taiwan (marked as A), SSH west of the northern tip of Luzon (marked as B) and SSH differences between A and B. Both the model results and the TOPEX/Poseidon data from the WOCE have been demeaned for comparing. In general, their variations have great resemblance in both except the intraseasonal fluctuations. In model results, the SSH at A had little variation; while at B it displayed clear annual and interannual variation. Consequently, the difference of SSH between A and B also showed annual and interannual variation. The variation of SSH differences correlates (correlation coefficient is 0.9) well with the modeled zonal transport across the Luzon Strait. The SSH difference varied from 0 to 26 cm. It could generate the zonal geostrophic transport having the same order of the modeled zonal transport across the Luzon Strait. Apparently, the meridional pressure gradient across the Luzon Strait was the primary factor causing the intrusion of Kuroshio. Qu (2000) and Metzger and Hurlburt (1996) had similar findings. However, the present finding indicates that the SSH difference was mainly due to low SSH north of Luzon. A conclusion, similar to the previous one, could be reached. The location and strength of South China Sea cyclonic flow (or low SSH center) has great impact on the Kuroshio intrusion across the Luzon Strait.

5. Discussion and summary:

Figure 16 shows the meridional volume transports in the upper 300 m water column south (along 18.5°N from 122°E to 125°E) and north (along 22.5°N from 121°E to 124°E) of the Luzon Strait, respectively. The former is treated as the transport of the upstream Kuroshio before it entered the Luzon Strait. The latter is regarded as the transport of Kuroshio after it left the Luzon Strait. The mean transports are 13.5 Sv and 15.7 Sv, respectively. These values are close to 14 Sv estimated by Qu et al. (1998) using repeated hydrographic sections near the Philippine coast. Both time series displayed large interannual and intraseasonal variation, but small annual variation. They were quite different characteristics than time series of zonal transport across the Luzon strait. The coherence between the meridional and zonal transport was low (not shown). The transport of upstream Kuroshio was greatest early in 1997. Theoretically, the swifter Kuroshio causes less zonal intrusion because of the larger inertia effect (Sheremet, 2001). Conversely, the zonal intrusion was greatest early in 1997. These results indicate that the variation of Kuroshio strength may have little impact on the zonal Kuroshio intrusion across the Luzon strait. It is noted that the meridional transport increased after it crossed the Luzon Strait. The eastward transport across the Luzon Strait in summer and the westward flow east of Kuroshio are mainly the sources for such increase.

The low SSH west of Luzon was primarily related to the wind stress curl, which was largest around November and smallest (turning to negative) around August. The positive wind stress curl caused the water divergence, depressed SSH and cooled upper ocean heat content. Liang et al. (2000) found that the correlation between the wind stress curl and upper 300 m ocean heat content in the South China Sea is highest (correlation coefficient is over 0.8) west of Luzon. However, the wind stress curl and upper 300 m ocean heat content was almost uncorrelated south of the Taiwan Strait. This could illustrate that the SSH had little seasonal variation south of Taiwan Strait while the wind stress curl did display seasonal variation. The pressure gradient (or even the Kuroshio intrusion) across the Luzon Strait is primarily caused by the low SSH center (South China Sea cyclonic flow) west of Luzon.

In summary, the current velocities, recorded by the three ADCPs in the Luzon Strait, indicate that the Kuroshio consistently intruded into the South China Sea through the central Luzon Strait. The observed current velocity had large intraseasonal, but small annual variation. The local wind is not the only factor causing these fluctuations. The observation validated the results of MICOM forced by the wind data provided by the ECMWF. The model confirmed that the Kuroshio intruded consistently into the South China Sea through the central Luzon Strait. The intrusion varied annually as well as interannually. The large interannual variation, which occurred in 1997-1998, made the annual variation indistinct and almost indiscernible in the observed current velocity. The Kuroshio intruded deeply into the South China Sea when the South China Sea cyclonic flow became a basin-wide feature, which primarily occurred during the northeast monsoon period. In the southwest monsoon period, the cyclonic flow was primarily confined to the northern South China Sea. The intruded Kuroshio was also confined to the northern South China Sea.

The zonal transport across the Luzon Strait varied annually, as well as interannually. It was primarily westward. Eastward transport was only observed in summer of certain years. When eastward transport occurred, the Kuroshio still intruded into the South China Sea but was weak. The current on the northern South China Sea shelf break flowing out of the South China Sea through the northern Luzon Strait exceeds the Kuroshio intrusion. The annual and interannual variations of zonal transport correlated with the meridional pressure gradient across the Luzon Strait. The pressure gradient varied primarily with the SSH west of northern Luzon. The wind stress curl is responsible for that SSH variation. The interannual variation of Kuroshio intrusion might have a cycle with El Niño.

Acknowledgements

This study was supported by the National Science Council, Taiwan, ROC, under grant NSC 89-2611-M-002-023-OP2, NSC 89-2611-M-002-031-OP2, and NSC 90-2611-M-012-001-OP2. The authors would like to acknowledge the RSMAS/MPO, University of Miami, for opening the source code of MICOM. The data processing and graphic plots have greatly benefited from the use of FERRET and GMT developed by NOAA's Pacific Marine Environmental laboratory and SOEST, University of Hawaii, respectively. The bathymetry and hydrographic data were offered by the Ocean Data Bank, National Center for Ocean Research, Taiwan, ROC. The assistance of the captain and crews of the R/V Ocean Researcher I are greatly appreciated. We also want to thank Mr. Wen-Hwa Ho for the mooring preparation.

References

Bleck, R., and L. T. Smith, 1990: A wind-driven isopycnic coordinate model of the North and Equatorial Atlantic Ocean. 1: Model development and supporting experiments. *J. Geophys. Res.*, **95**, 3273-3285.

——, C. Rooth, D. Hu, and L. T. Smith, 1992: Salinity-driven thermocline transients in a wind and thermohaline-forced isopycnic coordinate model of the North Atlantic. *J. Phys. Oceanogr.*, **22**, 1486-1505.

——, and E. Chassignet, 1994: Simulating the oceanic circulation with isopycnic-coordinate models. In: Majundar, S.K. (Ed.), The Oceans: Physical-Chemical Dynamics and Human Impact, 17-39.

Boulanger, J.-P., and C. Menkes, 1999: Long equatorial wave reflection in the Pacific Ocean from TOPEX/Poseidon data during the 1992-1998 period. *Climate Dyn.*, **15**, 205-225.

Chao, S.-Y., P.-T. Shaw, and S. Y. Wu, 1996: El Niño Modulation of the South China Sea Circulation. *Prog. Oceanogr.*, **38**, 51-93.

Chassignet, E. P., L. T. Smith, R. Bleck, and F. O. Bryan, 1996: A model comparison: Numerical simulations of the North Atlantic oceanic circulation in depth and isopycnic coordinates. *J. Phys. Oceanogr.*, **26**, 1849-1867.

Chu, P. C., and R. Li, 2000: South China Sea Isopycnal-Surface Circulation. *J. Phys.*

Oceanogr., **30**, 2419-2438.

Chuang, W.-S. and W.-D. Liang, 1994: Seasonal variability of intrusion of the Kuroshio water across the continental shelf northeast of Taiwan. *J. Oceanogr.*, **50**, 531-542

CPC/NCEP, 2002: El Niño/Southern Oscillation (ENSO) diagnostic discussion. NOAA, Climate Prediction Center/NCEP, MD, 1 pp

da Silva, A. M., C. C. Young, and S. Levitus, 1994: *Atlas of surface marine data 1994*. Vol. 1: *Algorithms and Procedures*. NOAA Atlas NESDIS 8, U.S. Department of Commerce, NOAA, NESDIS, 83 pp.

ECMWF, 1995: User Guide to ECMWF products. Meteorological Bulletin M3.2, 71 pp

Farris, A. and M. Wimbush, 1996: Wind-induced Kuroshio intrusion into the South China Sea. *J. Oceanogr.*, **52**, 771-784.

Hansen, D.V. and P.M. Poulain, 1996: Quality Control and Interpolation of WOCE/TOGA drifter data, *J. Atmos. Oceanic Technol.*, **13**, 900-909.

Kraus, E. B., and J. S. Turner, 1967: A one-dimensional model of the seasonal thermocline: II. The general theory and its consequence. *Tellus*, **19**, 98-106.

Kutsuwada, K. and M. J. McPhaden, 2002: Intraseasonal Variations in the upper equatorial Pacific Ocean prior to and during the 1997-98 El Niño. *J. Phys.*

Oceanogr., **32**, 1133-1149.

Levitus, S., 1982: *Climatological atlas of the World Ocean*. NOAA Professional Paper No. 13, U.S. Government Printing Office, Washington, DC, 173 pp.

——, and T. P. Boyer, 1994: *World Ocean Atlas 1994*. Vol. 4: *Temperature,* NOAA Atlas NESDIS, 117 pp.

——, R. Burgett, and T. P. Boyer, 1994, *World Ocean Atlas 1994*. Vol. 3: *Salinity*, NOAA Atlas NESDIS, 99 pp.

Liang, W.-D., J. C. Jan, and T. Y. Tang, 2000: Climatological wind and upper ocean heat content in the South China Sea. *Acta Oceanogr. Taiwanica* , **38**, 91-114.

——, T. Y. Tang, Y. J. Yang, M. T. Ko, and W.-S. Chuang, 2002: Upper ocean current around Taiwan. *Deep-Sea Res. Part II*. (accepted)

McPhaden, M. J., 1999: Genesis and evolution of the 1997-98 El Niño. *Science.*, **283**, 950-954.

——, and X. Yu, 1999: Equatorial waves and the 1997-98 El Niño. *Geophys. Res. Lett.*, **16**, 2961-1964.

Metzger, E. J., and H. E. Hurlbert, 1996: Coupled dynamics of the South China Sea, the Sulu Sea, and the Pacific Ocean. *J. Geophys. Res.*, **101**, 12 331-12 352.

Nitani, H., 1972: Beginning of the Kuroshio. In: *Kuroshio, its physical aspects*, H. Stommel and K. Yoshida, editors, University of Tokyo Press, Tokyo, 129-163.

NOAA, 1988: ETOPO5 digital relief of the Surface of the Earth. Data Announcement 88-MGG-02, NOAA, National Geophysical Data Center, Boulder, CO, 1 p.

Qiu, B., and R. Lukas, 1996: Seasonal and interannual variability of the North Equatorial Current, the Mindanao Current, and the Kuroshio along the Pacific western boundary. *J. Geophys. Res.*, **101**, 12 315-12 330.

Qu, T., H. Mitsudera, and T. Yamagata, 1998: On the western boundary currents in the Philippine Sea. *J. Geophys. Res.*, **103**, 7537-7548.

Qu, T., 2000: Upper-layer circulation in the South China Sea. *J. Phys. Oceanogr.*, **30**, 1450-1460.

Shaw, P.-T., 1991: The seasonal variation of the intrusion of the Philippine Sea Water into the South China Sea. *J. Geophys. Res.*, **96**, 821-827.

——, and S.-Y. Chao, 1994: Surface circulation in the South China Sea. *Deep Sea Res.*, **41**, 1663-1683.

——, ——, K.-K. Liu, S.-C. Pai, and C.-T. Liu, 1996: Winter Upwelling off Luzon in the Northeastern South China Sea. *J. Geophys. Res.*, **101**, 16 435-16 448.

Sheremet, V. A., 2001: Hysteresis of a western boundary current leaping across a gap. *J. Phys. Oceanogr.*, **31**, 1247-1259.

Stommel, H., and A. B. Arons, 1960: On the abyssal circulation of the world ocean - I. Stationary planetary flow patterns on a sphere. *Deep-Sea Res.*, **6**, 140-154.

Trenberth, K. E., J. G. Olson, and W. G. Large, 1989: A global ocean wind stress climatology based on ECMWF analyses, *NCAR Tech. NOTE*

NCAR/TN-338+STR, Natl. Cent. For Atmos. Res., Boulder, Colo., 93 pp.

Wang, J., and C. S. Chern, 1987: The warm-core eddy in the northern South China Sea, I. Preliminary observations on the warm-core eddy. *Acta Oceanogr. Taiwanica* , **18**, 92-103. (in Chinese with English abstract)

Wyrtki, K., 1961: Physical oceanography of the southeast Asian Waters, NAGA Rep. 2, Scripps Institution of Oceanography, La Jolla, CA , 195 pp.

Table Lists

TABLE 1. Mooring locations, instrument and water depths, and durations at L1, L2, and L3, respectively.

TABLE 1. Mooring locations, instrument and water depths, and durations at L1, L2, and L3, respectively.

Station	Location	Water depth	Instrument depth	Duration
L1	120° 56.0’E 20° 48.5’N	1288 m	282 m	1997/08/05-1997/09/12
L1	120° 56.4’E 20° 47.7’N	1313 m	290 m	1998/04/21-1998/06/11
L1	120° 56.4’E 20° 47.8’N	1319 m	328 m	1998/06/15-1999/04/07
L2	120° 54.5’E 20° 19.9’N	2057 m	193 m	1996/12/28-1997/08/05
L2	120° 54.3’E 20° 20.5’N	2011 m	199 m	1997/08/06-1997/09/12
L2	120° 54.9’E 20 19.7’N	2100 m	250 m	1998/06/15-1998/10/03
L3	120° 56.4’E 19° 48.7’N	1645 m	197 m	1996/12/28-1997/09/13

Figure Captions

Fig. 1. Locations of ADCP moorings (solid circle) and wind record station (asterisk) used in this study. The bathymetry is color shaded. It is overlaid on the composite Sb-ADCP current velocity vectors at 30 m from Liang et al. (2002). The reference vector is 100 cm s^{-1}. Regions A and B show the area of average used in Fig. 15.

Fig. 2. Time series of current velocity observed at L1. (a) *U* (dashed line), *V* (thick solid line) components and stick diagram (thin solid vector) of the depth-averaged (from 30 to 220 m) current velocity are shown. Vertical sections of (b) *U* and (c) *V* components of current velocity are shown in the middle and bottom panels, respectively. Contour interval is 50 cm s^{-1}. The time series was low-pass filtered to remove the fluctuations, for frequencies higher than 0.0139 cph.

Fig. 3. Same as Fig. 2 except at L2. The range of depth average is from 20 m to 120 m in 1997 and from 140 m to 240m in 1998.

Fig. 4. Same as Fig. 2 except at L3. The range of depth average is from 20 m to 160 m.

Fig. 5. T-S diagram at L1, L2, L3, the South China Sea, and the upstream Kuroshio: Dashed line: L1, dash-dotted line: L2, dotted line: L3, thin line: South China

Sea, and thick line: Kuroshio. The inset shows the locations.

Fig. 6. Northeast-southwest component wind velocity (thick line) at Lanyu Island is shown. The depth-averaged current velocity (same as Fig. 3a) at L2 is also shown. A 5-day convolution average was applied to both wind and current velocity.

Fig. 7. Domain of MICOM model used in this study. The land is shaded as black. The minimum depth of ocean is 50 m. Open ocean boundary includes about 4° sponge area.

Fig. 8. Comparisons between the monthly average velocity vectors of the observation (thick vector) and model result (thin vector) at (a) L1, (b) L2, and (c) L3 are shown.

Fig. 9. Comparisons between the depth-averaged current velocity of the observation and model result at (a) L1, (b) L2, and (c) L3 are shown. The thin and dotted lines are the *U* and *V* component of observed depth-averaged current velocity, respectively. The thick and dashed lines are the *U* and *V* component of model result, respectively. The ranges of depth average are the same as Fig. 2a, 3a, and 4a, except that a 5-day convolution average was applied to both observation and model results.

Fig. 10. Current velocity (vector stick) at 50 m and sea surface height (color filled

area) on 15th of (a) June and (b) December from the 10th spin up model results are shown.

Fig. 11. Same as Fig. 10 except for the results of the model started from the 10th spin up model results and continually forced by the 1997-2001 monthly mean momentum flux. Current velocities at depth 50m and SSHs in 1997-2001 are shown in (a)-(e), respectively. From top to bottom, it is shown for the 15th of March, June, September, and December.

Fig. 12. (a) Depth-averaged *U* in the upper 300 m water column, (b) SSH of model results along 120.75°E from 18.5°N to 22°N are shown. A 5-day convolution average was applied to both. Shaded areas show the positive value. Contour intervals are 10 cm s^{-1} and 5 cm in (a) and (b), respectively. The 3 straight lines indicate mooring locations.

Fig. 13. Zonal volume transport along 127.5°E of model results in the upper 300 m water column between 18.5°N and 22°N is shown. A 5-day convolution average was applied. Negative and positive values represent the westward and eastward transport, respectively.

Fig. 14. Time series of (a) northeast-southwest component of ECMWF wind stress at L2 and (b) zonal Ekman volume transport along 120.75°E between 18.5°N and 22°N. A 30-day convolution average was applied to all.

Fig. 15. Time series of (a) SSH at A , (b) SSH at B, (c) the SSH difference between A and B. Both the model result (solid line) and the T/P data (dashed line) have been demeaned. A 5-day convolution average was applied to all. The locations of A and B are show in Fig. 1.

Fig. 16. Meridional volume transports in the upper 300 m water column (a) along 18.5°N from 122°E to 125°E and (b) along 22.5°N from 15°N to 18°N of model results are shown. A 5-day convolution average was applied to both.

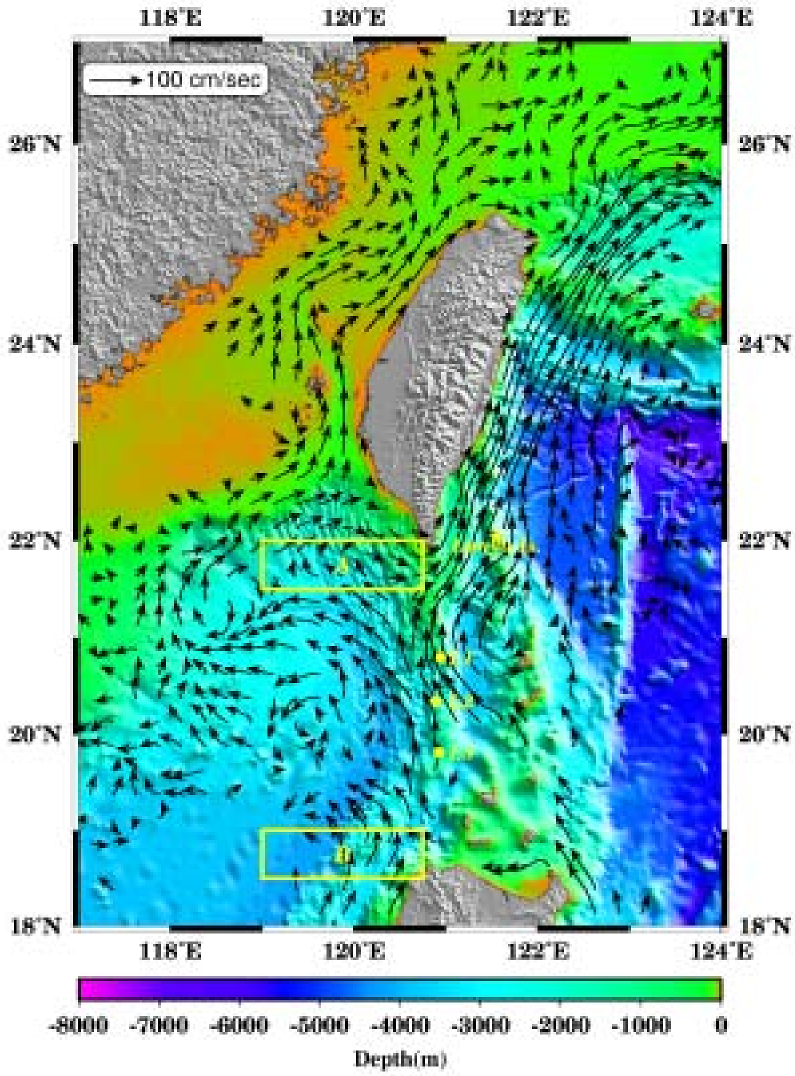

Fig. 1. Locations of ADCP moorings (solid circle) and wind record station (asterisk) used in this study. The bathymetry is color shaded. It is overlaid on the composite Sb-ADCP current velocity vectors at 30 m from Liang et al. (2002). The reference vector is 100 cm s^{-1}. Regions A and B show the area of average used in Fig. 15.

Fig. 2. Time series of current velocity observed at L1. (a) U (dashed line), V (thick solid line) components and stick diagram (thin solid vector) of the depth-averaged (from 30 to 220 m) current velocity are shown. Vertical sections of (b) U and (c) V components of current velocity are shown in the middle and bottom panels, respectively. Contour interval is 50 cm s^{-1}. The time series was low-pass filtered to remove the fluctuations, for frequencies higher than 0.0139 cph.

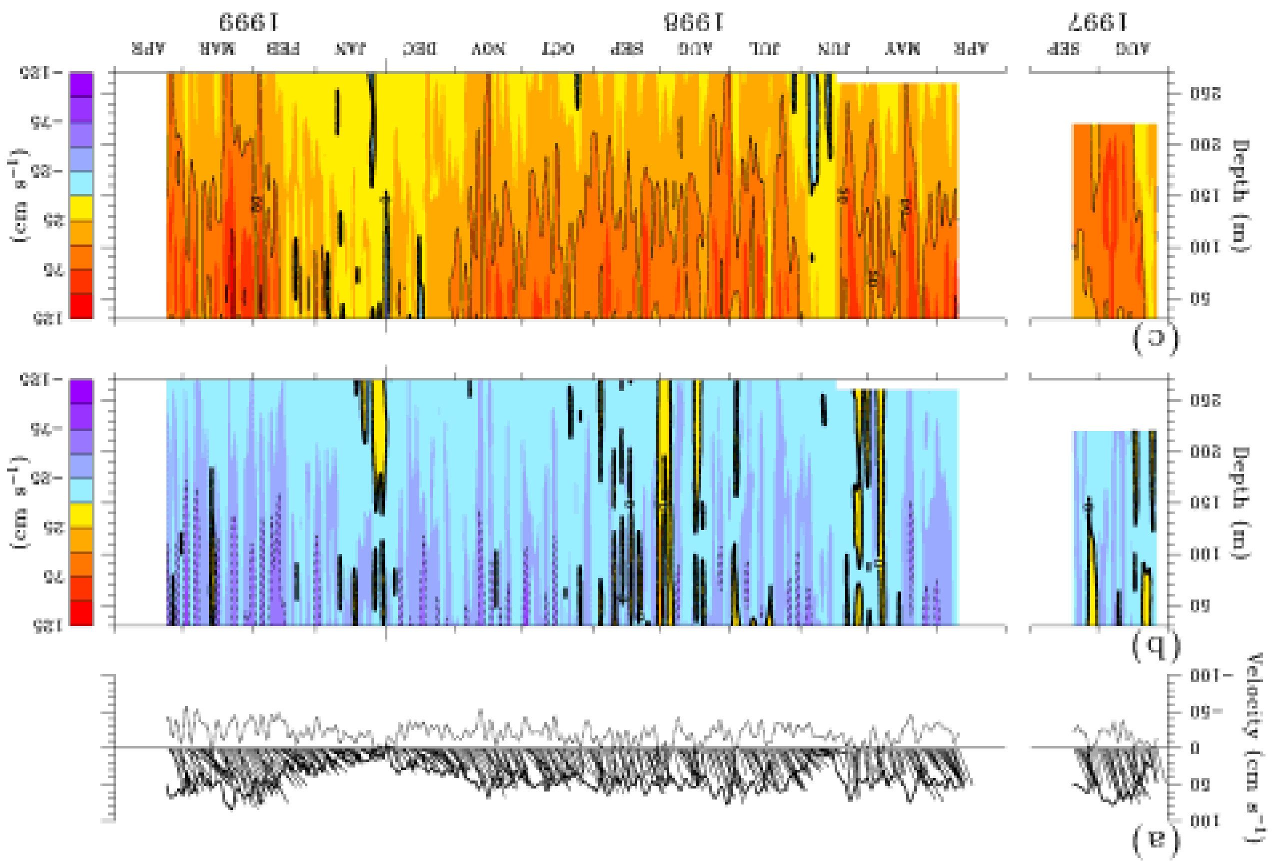

Fig. 3. Same as Fig. 2 except at L2. The range of depth average is from 20 m to 120 m in 1997 and from 140 m to 240m in 1998.

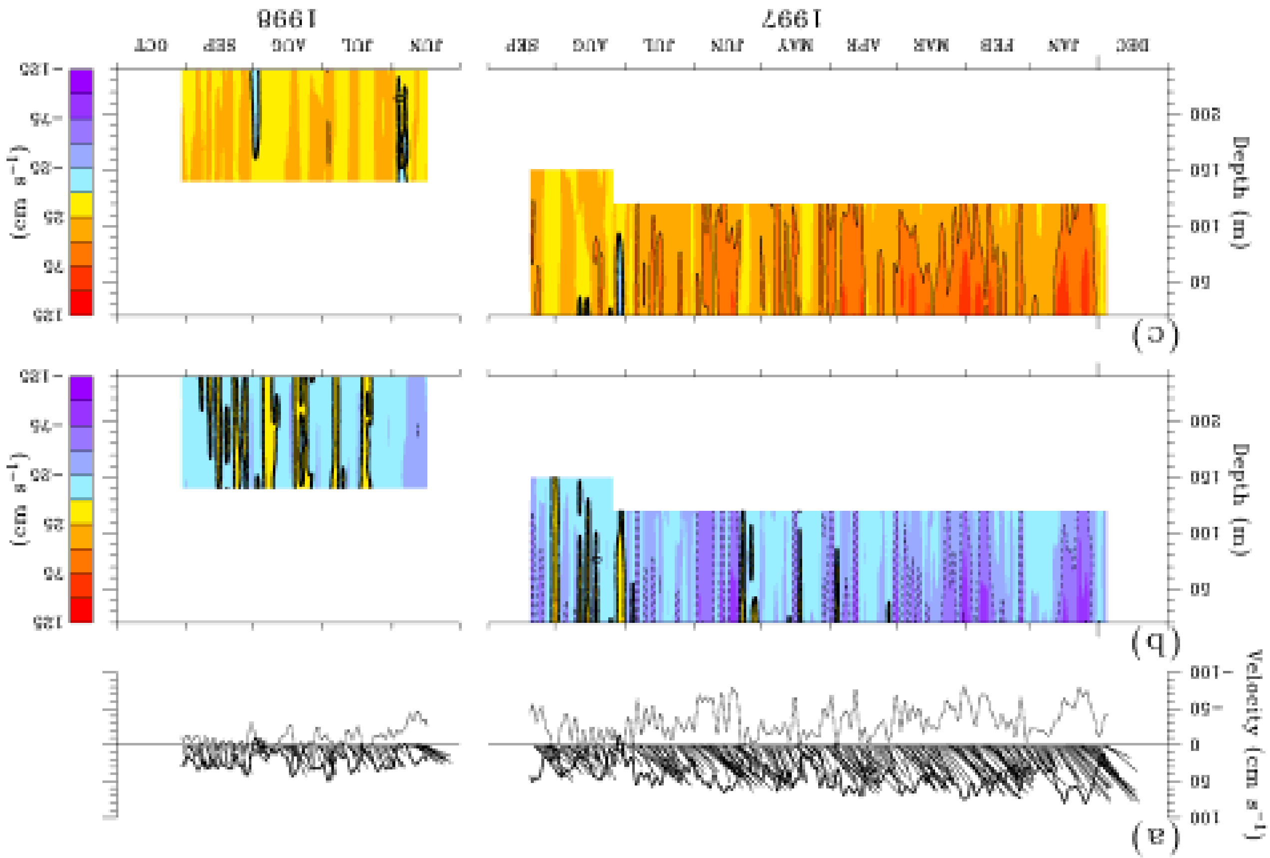

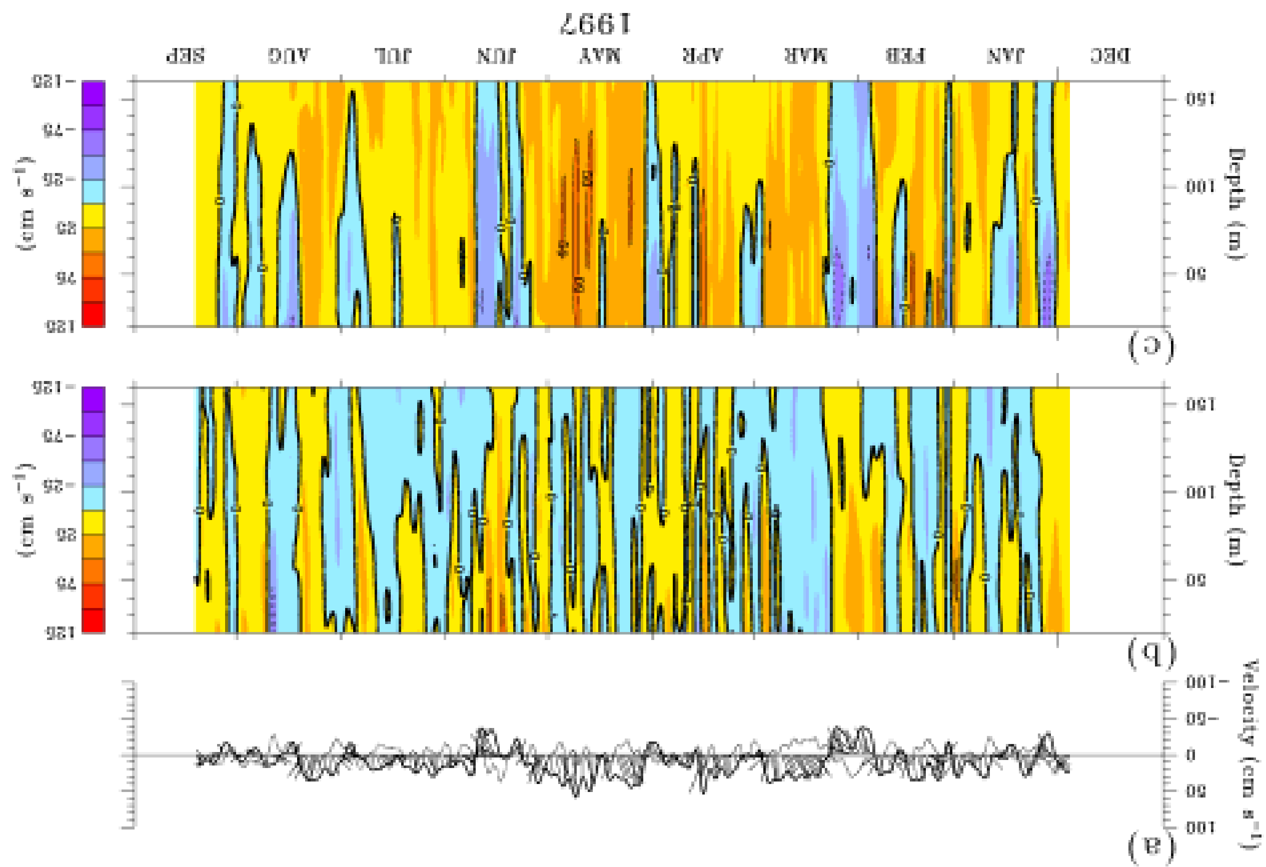

Fig. 4. Same as Fig. 2 except at L3. The range of depth average is from 20 m to 160 m.

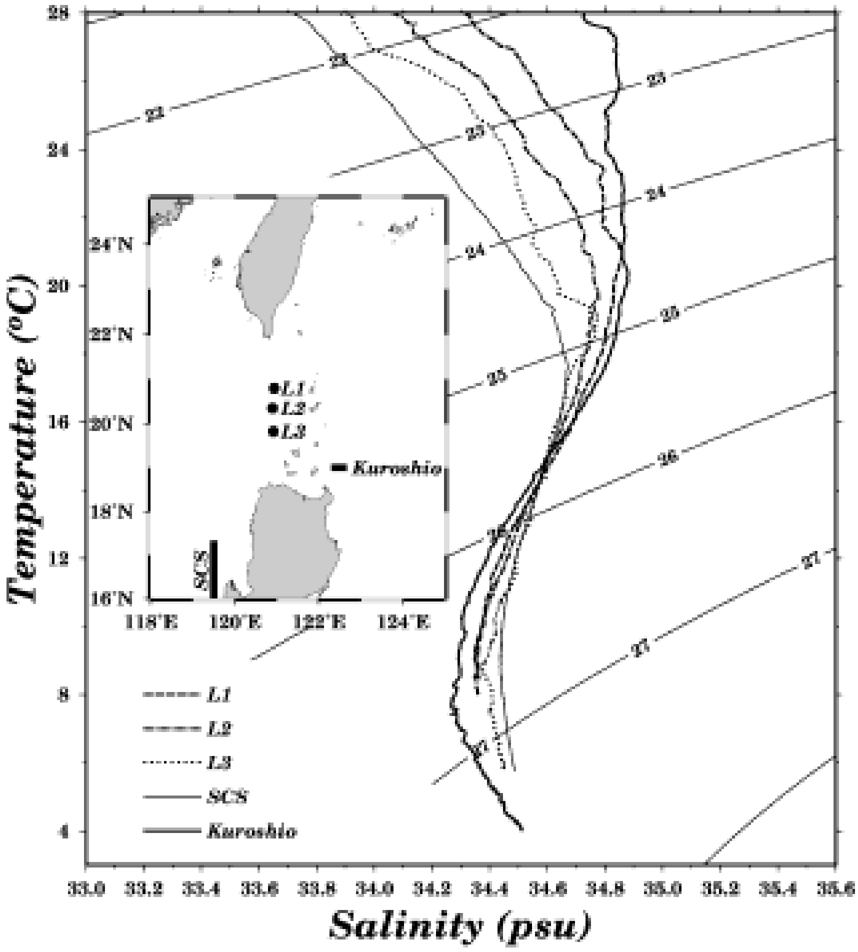

Temperature (°C)
Salinity (psu)
28
24
20
16
12
8
4
33.0
33.2
33.4
33.6
33.8
34.0
34.2
34.4
34.6
34.8
35.0
35.2
35.4
35.6
22
23
24
25
26
27
24°N
22°N
20°N
18°N
16°N
118°E
120°E
122°E
124°E
L1
L2
L3
Kuroshio
SCS
L1
L2
L3
SCS
Kuroshio

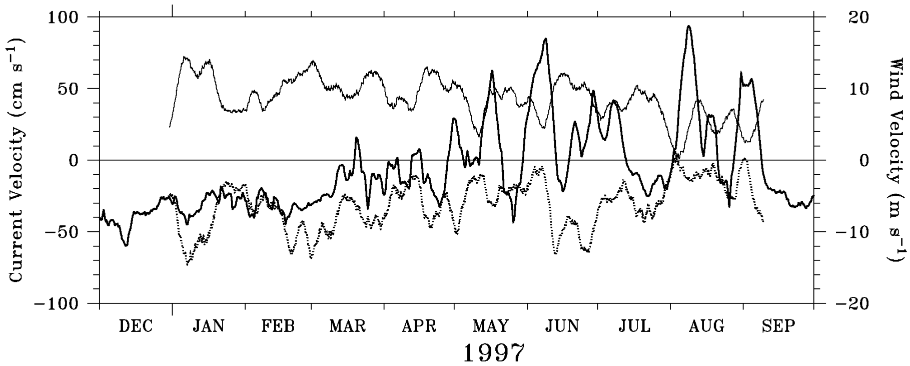

Fig. 6. Northeast-southwest component wind velocity (thick line) at Lanyu Island is shown. The depth-averaged current velocity (same as Fig. 3a) at L2 is also shown. A 5-day convolution average was applied to both wind and current velocity.

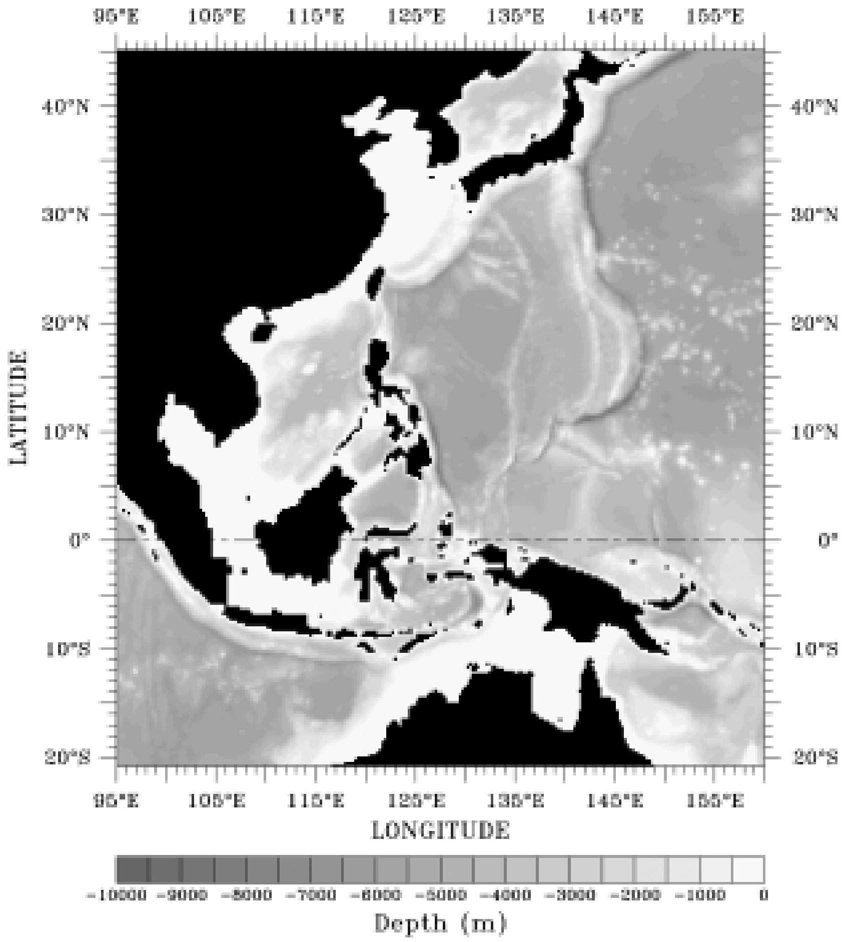

Fig. 7. Domain of MICOM model used in this study. The land is shaded as black. The minimum depth of ocean is 50 m. Open ocean boundary includes about 4° sponge area.

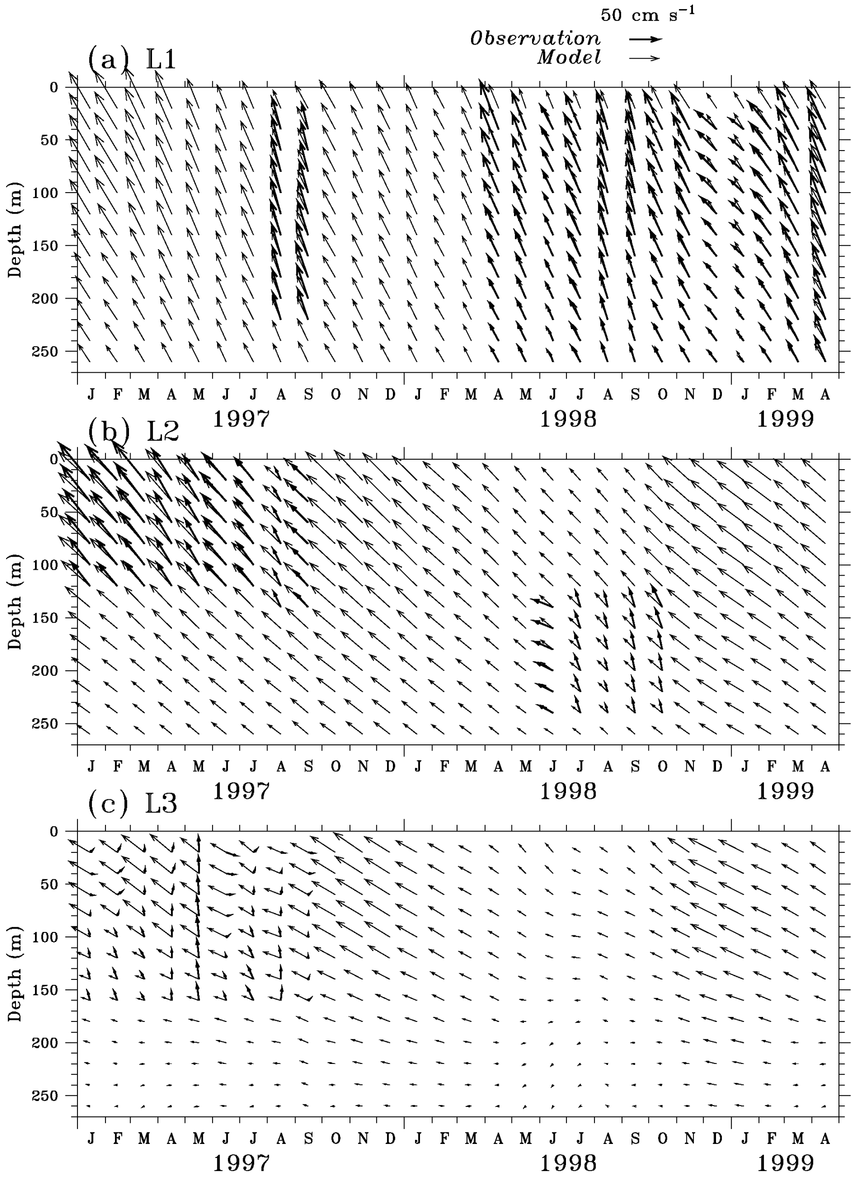

Fig. 8. Comparisons between the monthly average velocity vectors of the observation (thick vector) and model result (thin vector) at (a) L1, (b) L2, and (c) L3 are shown.

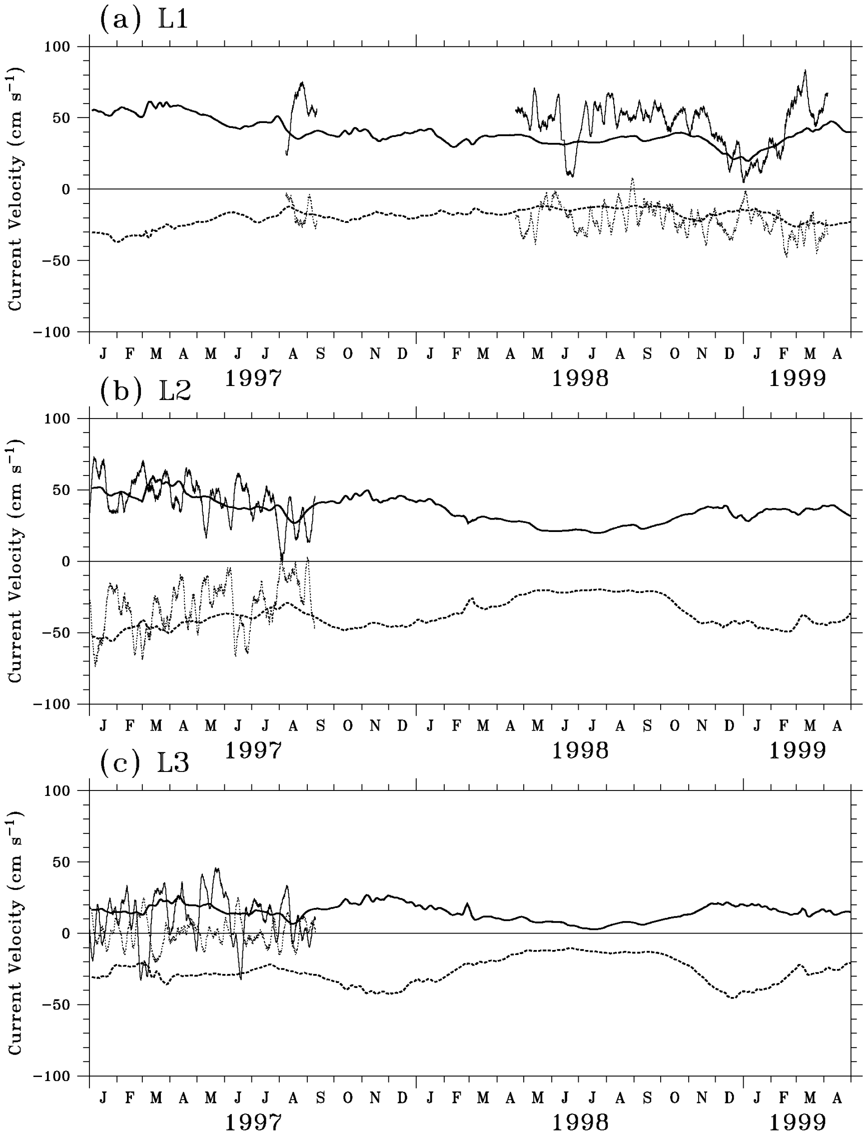

Fig. 9. Comparisons between the depth-averaged current velocity of the observation and model result at (a) L1, (b) L2, and (c) L3 are shown. The thin and dotted lines are the *U* and *V* component of observed depth-averaged current velocity, respectively. The thick and dashed lines are the *U* and *V* component of model result, respectively. The ranges of depth average are the same as Fig. 2a, 3a, and 4a, except that a 5-day convolution average was applied to both observation and model results.

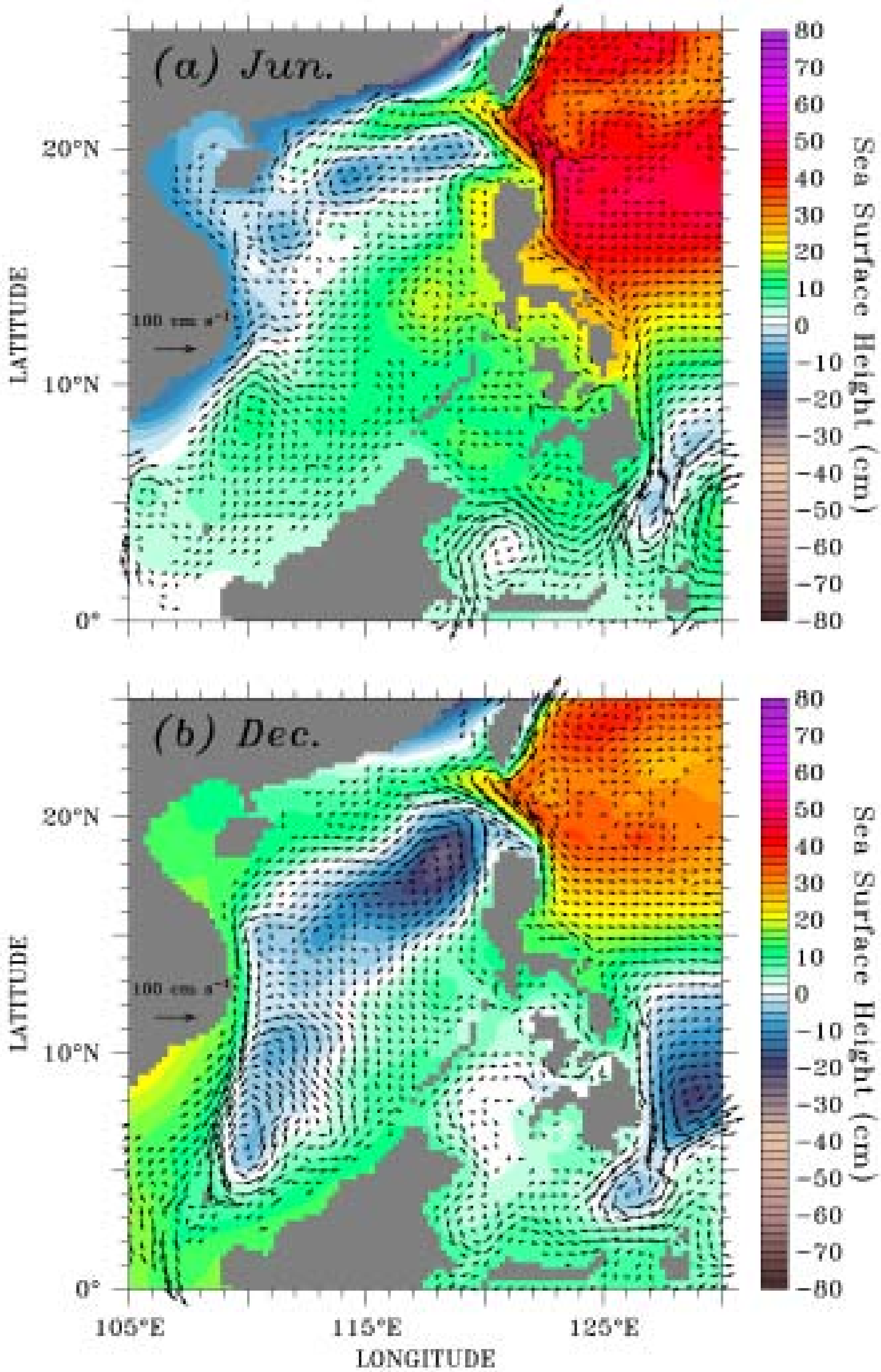

Fig. 10. Current velocity (vector stick) at 50 m and sea surface height (color filled area) on 15th of (a) June and (b) December from the 10th spin up model results are shown.

Fig. 11. Same as Fig. 10 except for the results of the model started from the 10th spin up model results and continually forced by the 1997-2001 monthly mean momentum flux. Current velocities at depth 50m and SSHs in 1997-2001 are shown in (a)-(e), respectively. From top to bottom, it is shown for the 15th of March, June, September, and December.

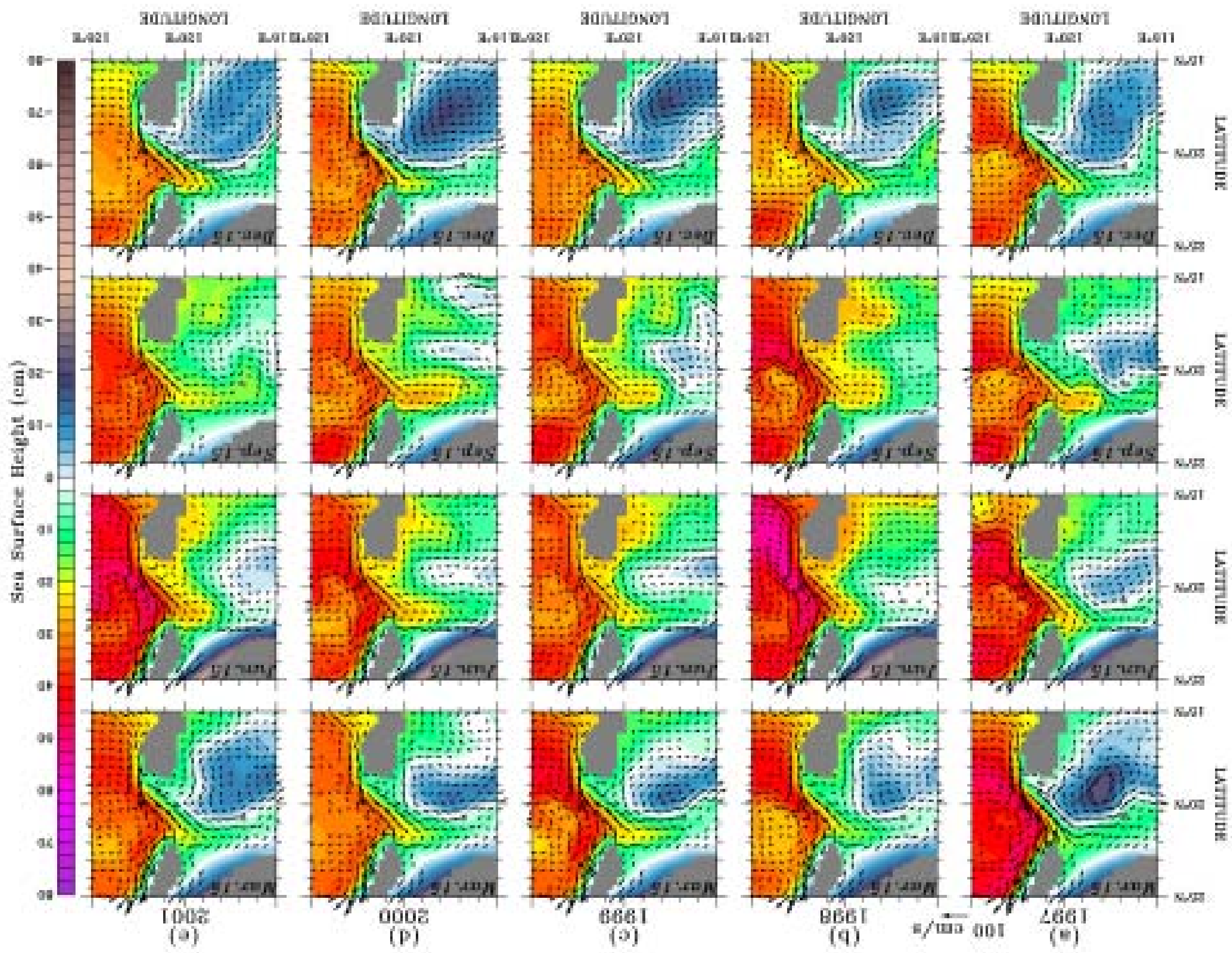

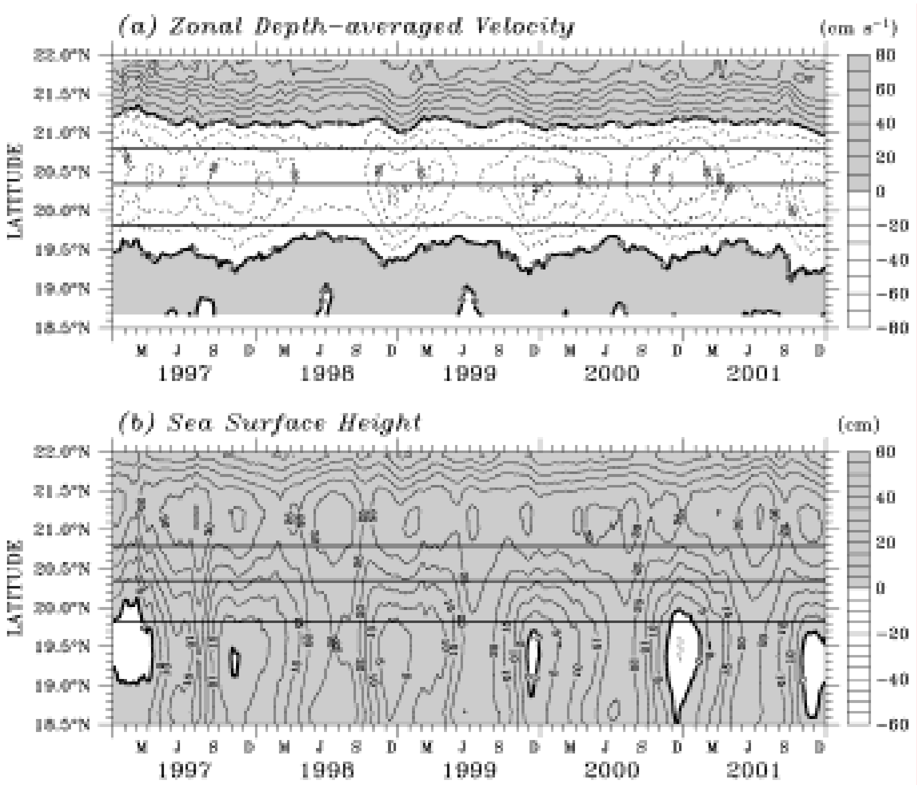

Fig. 12. (a) Depth-averaged *U* in the upper 300 m water column, (b) SSH of model results along 120.75°E from 18.5°N to 22°N are shown. A 5-day convolution average was applied to both. Shaded areas show the positive value. Contour intervals are 10 cm s^{-1} and 5 cm in (a) and (b), respectively. The 3 straight lines indicate mooring locations.

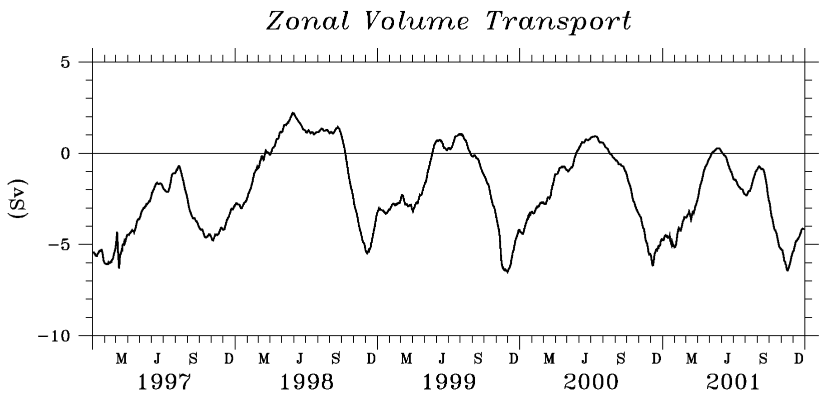

Fig. 13. Zonal volume transport along 127.5°E of model results in the upper 300 m water column between 18.5°N and 22°N is shown. A 5-day convolution average was applied. Negative and positive values represent the westward and eastward transport, respectively.

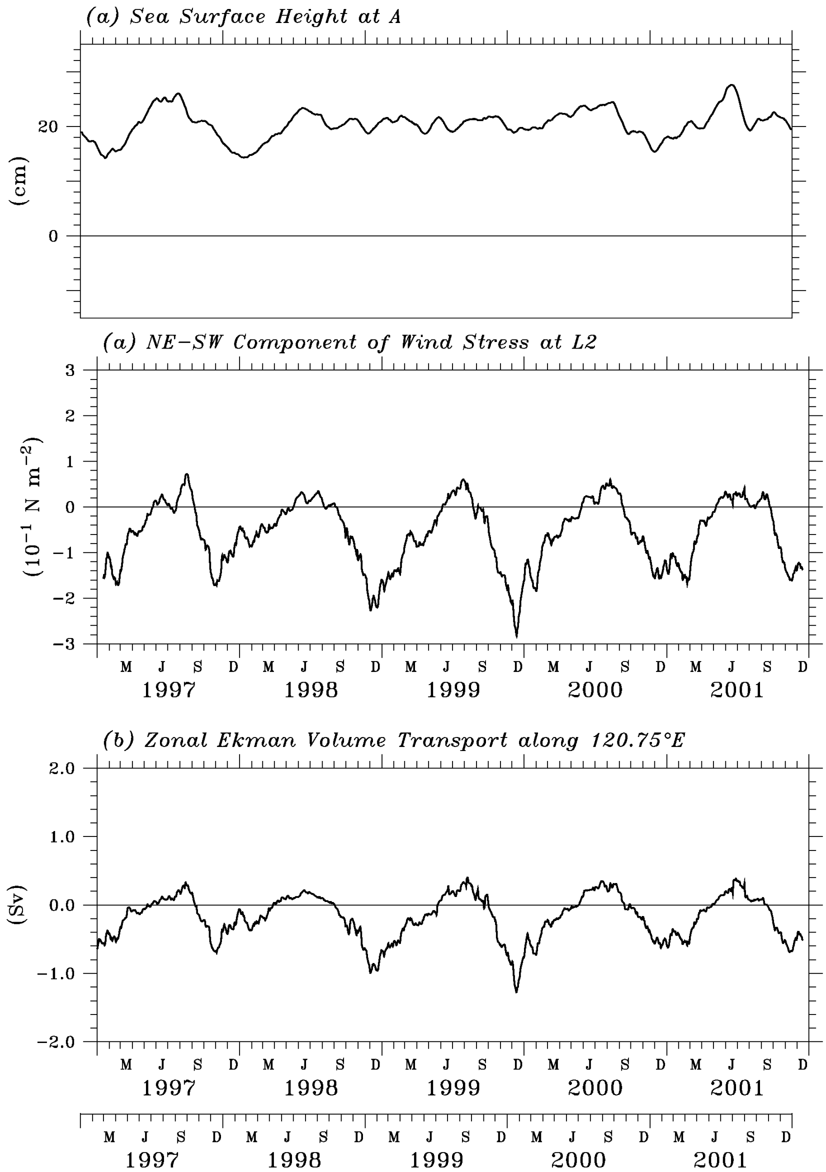

Fig. 14. Time series of (a) northeast-southwest component of ECMWF wind stress at L2 and (b) zonal Ekman volume transport along 120.75°E between 18.5°N and 22°N. A 30-day convolution average was applied to all.

Intra-seasonal variation in the velocity field of the northeastern South China Sea

Chau-Ron Wu[1], T. Y. Tang[2,*], S. F. Lin[2,3], Y. J. Yang[4], and W.-D. Liang[4]

[1]*Department of Earth Sciences, National Taiwan Normal University, Taipei, Taiwan, ROC*

[2]*Institute of Oceanography, National Taiwan University, Taipei, Taiwan, ROC*

[3]*Energy & Resources Laboratories, Industrial Technology Research Institute, Hsinchu, Taiwan, ROC*

[4]*Department of Marine Science, Chinese Naval Academy, Kaohsiung, Taiwan, ROC*

[*]***Corresponding author. Institute of Oceanography, National Taiwan University, P.O. Box 23-13, Taipei, 106, Taiwan, ROC, Tel: +886-2-23626097; Fax: +886-2-23698526; Email address: tyt@ccms.ntu.edu.tw***

Submitted to

Geophysical Research Letters

November, 2003

Abstract

Two subsurface ADCPs were deployed at the northeastern South China Sea to study circulation structure in the area and path of Kuroshio intrusion. The 48-hour low-pass filtered data reveal significant intra-seasonal variations in the velocity field. The current alternates between clockwise and counterclockwise even within a single month. Local wind stress forcing fails to address the phenomena and variations. The present study suggests wind stress curl forcing is the dominant process controlling the circulation picture. While a stronger curl developed off southern tip of Taiwan, it will provide negative vorticity to the intruded current and form an anticyclonic eddy. The stronger current is always going along with the stronger curl. On the other hand, while the curl looses or decays, the intruded current becomes weakened and forms a cyclonic eddy. The agreement between curl and velocity suggests that changes in the curl contribute to the intra-seasonal variations in the region.

Introduction

The circulation structure in the northeastern South China Sea (SCS) is extremely complicated. In addition to the location with a complicated topography and seasonal reversal monsoon, the regions might be interacted between currents from both northern SCS and Taiwan Strait. Furthermore, it is well known that the Kruoshio front might reach the sea southwest of Taiwan and influence the shelf break circulation [*Fan and Yu*, 1981]. All of these factors induce varieties of contributions and alter the current structures in the regions. Especially the intrusion current from Kuroshio front, it might be the most important component and be the major theme in the area.

The Pacific western boundary current, the Kuroshio, flows northward and bypasses east of Luzon and Taiwan. Similar to the Loop Current in the Gulf of Mexico, the Kuroshio water has also been reported to intrude the Luzon Strait where plays a deep gap in the western boundary. Seasonal variations of Kuroshio intrusion have been reported extensively in a wealth of existing literature [e. g. *Wyrtki*, 1961; *Shaw*, 1991]. However, the conclusion of seasonal intrusion is challenged by several recent observations. For example, both moored current data and ship-board Acoustic Doppler Current Profiler (ADCP) data evidenced that the westward trend of Kuroshio intrusion is persisted all the year round [*Liang et al*., 2003; *Tang et al*., 2003].

Furthermore, although the intrusion of waters from the Kuroshio to the northeastern SCS has been studied for several decades, the path and process of Kuroshio intrusion in the region remained discrepancies among oceanographers. For example, based on hydrographic data, *Wang and Chern* [1987] inferred an anticyclonic (clockwise) eddy occupied the area at the onset of the northeast monsoon. Also based on hydrographic data in May and August 1986, on the other hand, *Shaw*

[1989] suggested that the intrusion current was probably part of a cyclonic (counterclockwise) circulation in the northern SCS. Anticyclonic or cyclonic circulation is of importance to the distribution of the water masses in the region. A correct description of circulation pattern is essential to future dynamic studies of the intrusion process.

In this study, current and hydrographic data from two mooring stations were examined to study the circulation pattern in the region. The direct observations in the velocity field are capable of determining the distribution of the Kuroshio intrusion water and inferring the path of intrusion. The results show that significant intra-seasonal variations in the velocity field. The current pattern alternates between clockwise and counterclockwise. Wind stress curls were also calculated from the blended QSCAT/NCEP wind stress fields at a resolution of 0.5° x 0.5° [*Milliff et al.*, 1999] to examine the driving mechanism of the local current.

Mooring data

Two sets of subsurface moorings (named St. W and St. E) were deployed in the west and east of the shelf break of the northeastern SCS, respectively. Figure 1 shows the mooring locations and the surrounding bathymetry. Each set of mooring includes an upward-looking, 150 *kHz*, self-contained ADCP mounted on a 45” diameter spherical syntactic foam buoy and a SEACAT Conductivity-Temperature-Depth (CTD) mounted 5 *m* beneath the ADCP. The water depths at St. W and St. E are 1014 *m* and 968 *m*, respectively. Table 1 lists the locations and local water depths for each mooring, the depths of instruments, the duration of deployments, and the vertical range of current profile measured by the ADCP. The bin length of ADCP was set as 8 *m*. The hourly current velocity was recorded averaged over 240 pings for board-band ADCP. The standard deviations of measurement velocity were 1.2 $cm\ s^{-1}$. The obtained current velocity of ADCP was corrected for vertical excursion and sound speed by the CTD data. The data were also adjusted for local magnetic deviation. Finally, the vertical profile of current velocity was linearly interpolated and resampled at 10 *m* intervals. The time series of current velocity discussed in the following sections were low-pass filtered to remove the fluctuations for frequencies higher than 0.5 cycles per day.

Results and discussion

Low-pass filtered velocity

Figure 2 shows the eastward (U) and northward (V) components of 48-hour low-pass filtered current velocity at St. W. Graphically, both U and V show significant intra-seasonal variations. By November 2000, U is weak and alternates directions between westward and eastward. The current enhances and turns eastward in December, reaching its maximum strength in the end of December. Just in the beginning of January, the eastward current decreases suddenly and reverses thereafter. Until March 2001, a repeat behavior takes place when eastward flow appears in the middle of March and reaches its maximum in the end of the month, turning westward suddenly afterward. Similar pattern is presented in the V. In the end of both December 2000 and March 2001, the V turns southward after it accelerated northward.

Similar to Figure 2, Figure 3 shows U and V of low-pass filtered velocity at St. E. Significant intra-seasonal variations are also evidenced at St. E. Graphically, U is generally weak except in October, November 2000 and February 2001 when stronger currents with speed more than 50 $cm\ s^{-1}$ occur and all of them flow eastward. Two periods of weak westward currents present in January and after middle March 2001. Frequently reversal currents are shown in V. Prior to middle of December, currents flow southward mostly, turning northward thereafter. Stronger southward currents show again in the middle of February, reaching its maximum speed of 100 $cm\ s^{-1}$ on March 1, 2001. The current turns northward in the middle of March and persists into April. Furthermore, the intra-seasonal variation at St. E seems to agree well with that at St. W, indicating that St. E and St. W are related to each other somehow. To emphasize this, the stick plots of depth average at St. W (20-130 *m*) and St. E (20-180 *m*) are shown together in Figure 4. Similar intra-seasonal reversals of currents between St. W and St. E come to the first sight. However, it seems that changes in St.

E generally lead those in St. W around 10~15 days. The phenomenon deserves to further verify and will be examined in detail in the next section.

In Figure 4, northward flow prevails at St. W and southeastward flow exists at St. E prior to the middle of December 2000. The feature infers that this region is dominated by a conceptual clockwise circulation pattern. Currents at St. W reverse southwestward and meanwhile currents at St. E turn either northwestward or northeastward during the period from middle December to middle February. The reversal phenomena suggest that current pattern alters from clockwise circulation to counterclockwise in the study region. Clockwise circulation dominates again during the period from middle February to middle March. Note that the currents are always stronger during clockwise circulation. After March, weak counterclockwise circulation plays the finale. Furthermore, as mentioned in the introduction section, currents perform an anticyclone or a cyclone might directly influence the geographic distribution of the water masses in the region. Without a correct description of circulation pattern, it is not possible to identify the water masses and to verify the intrusion process.

Water masses and circulation pattern

To describe the distribution of various water masses and the path of Kuroshio intrusion, the mooring CTD data at both St. W and St. E were plotted in Figure 5.

Also join with velocity vectors to separate different episodes of clockwise and counterclockwise circulation. In the figure, the red color represents clockwise circulation while the blue represents counterclockwise circulation. Temperature and salinity of St. W and St. E were measured at depth of around 160 *m* and 205 *m*, respectively. Although the absolute values of CTD data are probably problematic, the relative value can still be applied to identify where the water masses come from. Since not only temperature but salinity of St. E are generally lower than those of St. W, the measured depth at St. E is deeper could not account for the phenomena singly. Rather, there must be colder and fresher water entering and mixing with the local water around regions of St. E. Based on long-term mooring observations around sea southwest of Taiwan, mean current always flows southeastward during winter [*Chern*, 1982]. With mixing cold and fresh coastal water from Taiwan Strait, it makes sense that temperature and salinity at St. E should be lower than those at St. W.

Furthermore, concerning the temporal variability in each station, both stations show that temperature is higher whenever clockwise circulation dominates in the region. The temperature difference is more distinct at St. W where is far away from influence of colder coastal water. The higher values of temperature were presented in December 2000 and March 2001. The results are reasonable and can be explained by water movement. Currents generally intensify while clockwise circulation performs as mentioned earlier so that stronger intrusion current brings in warmer water from Kuroshio front and then increases water temperature at St. W. On the other hand, during counterclockwise circulation episode (e.g. in the middle of January), the current is weak and flows westward continuously along its northern boundary in Taiwan Strait. By gradually mixing with cold front from Taiwan Strait, the water temperature decreases.

To further study alternation of circulation pattern and relation between St. W and St. E, we rotated the current velocity to its principal axis. The principal axis of St. W is 45° clockwise-rotated Cartesian (northeastern-southwestern) and St. E is 135° clockwise-rotated Cartesian (southeastern-northwestern). Figures 6a and 6b show time series of principal axis depth-average current velocity at St. W and St. E, respectively. Graphically, both St. W and St. E evidence two significant peaks. However, the timing is not consistent with each other. Two peaks at St. W are during the periods December and March while at St. E are from middle November to middle December and from middle February to middle March. The results demonstrate that St. E leads St. W and an interval of 315-hour might properly describe time lag of St. W. In Figure 6c, St. E with time lag of 315 hours is overlapped to St. W. Peak-to peak comparison indicates that the variations of St. W and those in time lag of St. E are frequently in phase, suggesting St. E leads St. W by 10~15 days indeed. The trend is always valid whatever during episode of clockwise or counterclockwise circulation. The fact that St. E leads St. W during clockwise episode is probably against intuitive. Therefore, not merely a single anticyclone structure might be inferred and be expected.

Mechanism

What causes the intra-seasonal variation in the area deserves to further investigate. Intuitively, currents in the area, especially those near surface currents, should be driven by the strong monsoon during winter when northeasterly winds prevail. However, there is almost no correlation between the current and local wind forcing from weather station at Tung-Chi Island (figure not shown). Based on model simulations in the South China Sea, *Wu et al*. [1998] suggested that the formation of a gyre, whatever anticyclonic or cyclonic, is essential determined by the wind stress curl. *Shaw et al*. [1999] also found that the first two empirical orthogonal functions (EOF) modes of the wind stress curl agree well with those in the corresponding altimeter sea level modes, further supporting the wind stress curl forcing scenario. However, it is not clear whether the wind stress curl is also important to meso-scale circulation as in the present study. We adopted 6-hourly maps of 10 *m* zonal and meridional wind components at a resolution of 0.5° x 0.5°, which is derived from a space and time blend of QSCAT-DIRTH satellite scatterometer observations and

NCEP analyses [*Milliff et al*., 1999]. Wind stress curls are calculated from these blended wind stress fields. Figure 7 shows the monthly mean of the wind stress curl during the six-month period. The days in February and March 2001 have been slightly adjusted to fit the intra-seasonal variation in the velocity field. Main features in the intra-seasonal variation of the wind stress curl are captured in the sequence of plots from (a)-(f). In October 1999 (Figure 7a), a dipole structure with positive value to the north appeared in the region. Note that the south portion is what we should be more concern about since its position approaches the Kuroshio intrusion. Off southern tip of Taiwan, the large and negative curl extends southwestward in October that marks the onset of the winter monsoon. The pattern persists well into November, gradually increasing its strength in December. In the following month, the southern curl weakens (Figure 7d). The curl increases again and reaches its maximum strength during the period from February 10 to March 10 (Figure 7e) and decays afterwards (Figure 7f). The variations of the southern curl are corresponding to those shown in the velocity field and the curl is capable of explaining the intra-seasonal variations in the velocity field. While the southern curl appeared and developed in the position, the intruded current from Kuroshio would form anticyclonic eddies clockwise because the curl provides negative vorticities to the current. Note that the strongest southern curl is confined and limited near St. E. Therefore, a tight and stronger anticyclone might occur in close vicinity of St. E merely. The loosed clockwise vortexes might shed away from St. E while the corresponding Reynolds number is large enough. The large value of curl also explains the reason why the current is accelerated during clockwise circulation dominated episode as mentioned earlier. For example, the strongest southward current at St. E with maximum speed of 100 $cm\ s^{-1}$ shown on March 1, 2001 is well corresponding to the strongest southern curl in Figure 7e. On the other hand, while the southern curl weakens or looses (Figure 7d, 7f), the intruded current overwhelms the curl and continues westward along the shelf break, forming a weak cyclonic (counterclockwise) eddy. Weaker currents in these two counterclockwise episodes are also noted in the previous section.

Summary and Conclusions

Although the East Asian monsoons dominate, an intra-seasonal instead of seasonal variation in the velocity field has been found in the region. The agreement between wind stress curl and velocity fields suggests that the wind stress curl could be the main driving force to trigger the intra-seasonal variations. The intensity of wind stress curl off southern tip of Taiwan could determine whether clockwise or counterclockwise circulation pattern performs in the region. While the southern curl enhanced, the intruded current strengthens by getting large vorticity from the curl and forms an anticyclonic eddy afterwards. The mooring velocity data indeed evidence that currents during clockwise circulation are much stronger than those during counterclockwise. Temperature is also higher while clockwise since the stronger intrusion current will bring in Kuroshio warmer water and increase local water temperature.

Acknowledgements

We would like to thank Mr. Y. C. Tsai for processing the mooring data. This research was supported by the National Science Council, Taiwan, ROC, under grants NSC 89-2611-M-002-031-OP2 (TYT), NSC 91-2611-M-003-004 (CRW), and NSC 90-2611-M-012-001-OP2 (YJY).

References

Chern, C. S., Current and wave measurement in the vicinity of Hsien-Da-Kang and Tung- Kang (continued), *Special Pub. 39*, Inst. of Oceanogr., Natl. Taiwan Univ., Taiwan, 1982.

Fan, K. -L., and C.-Y. Yu, A study of water masses in the seas of south most Taiwan, *Acta Oceanogr. Taiwan.*, **12**, 94-111, 1981.

Liang, W.-D., T. Y. Tang, Y. J. Yang, M. T. Ko, and W.-S. Chuang, Upper-ocean current around Taiwan, *Deep-Sea Res. II,* **50**, 1085-1105, 2003.

Milliff, R. F., W.G. Large, J. Morzel, G. Danabasoglu, and T. M. Chin, Ocean general circulation model sensitivity to forcing from scatterometer winds, *J. Geophys. Res.*, **104**, 11337-11358, 1999.

Shaw, P.-T., The intrusion of water masses into the sea southwest of Taiwan, *J. Geophys. Res.*, **94**, 18213-18226, 1989.

Shaw, P. –T., The seasonal variation of the intrusion of the Philippine Sea water into the South China Sea, *J. Geophys. Res.*, **96**, 821-827, 1991.

Shaw, P.-T., S.-Y. Chao, and L.-L. Fu, Sea surface height variations in the South China Sea from satellite altimetry, *Oceanol. Acta*, **22**, 1-17, 1999.

Tang, T. Y., W.-D. Liang, Y. J. Yang, and W.-S. Chuang, Kuroshio intrusion in the Luzon Strait, *J. Phys. Oceanogr.*, submitted, 2003.

Wu, C.-R., P.-T. Shaw, and S.-Y. Chao, Seasonal and interannual variations in the velocity field of the South China Sea, *J. Oceanogr.*, **54**, 361-372, 1998.

Wang, J. and C. S. Chern, The warm-core eddy in the northern South China Sea, Preliminary observations on the warm-core eddy, *Acta Oceanogr. Taiwan.*, **18**, 92-103, 1987.

Wyrtki, K., Physical oceanography of the southeast Asian waters, Scientific Results of Marine Investigation of the South China Sea and the Gulf of Thailand, *NAGA Report Vol. 2*, 195 pp., Scripps Institution of Oceanography, La Jolla, California, 1961.

TABLE 1. Mooring locations; water, ADCP and CTD depths; durations; and data distribution depths (interval of 10 *m*) at St. W and St. E, respectively.

Station	Longitude	Latitude	Water Depth	ADCP Depth	CTD Depth	Duration	Measurement Range
St. W	118° 44’E	22°N	1014 *m*	160 *m*	165 *m*	2000/10/13~ 2001/04/18	20~130 *m*
St. E	120° 10’E	22°N	968 *m*	202 *m*	207 *m*	2000/10/04~ 2001/04/18	20~180 *m*

Figure Captions

Figure 1. The study area with locations of mooring stations (squares) and Tung-Chi Island (asterisk). The current distribution at 30 m is adopted from *Liang et al*. [2003].

Figure 2. Vertical sections of 48-hr low-pass current velocity observed at St. W. Contour interval is 10 $cm\ s^{-1}$.

Figure 3. Same as Figure 2 except at St. E.

Figure 4. Stick plots of the depth-averaged current velocity at St. W and St. E, respectively.

Figure 5. T-S diagram at St. W and St. E. Velocity vectors are also presented to separate different episodes of clockwise (red) and counterclockwise (blue) circulation.

Figure 6. Time series of principal axis depth-average current velocity at St. W and St. E, respectively. St. E with time lag of 315 hours is overlapped to St. W shown in the bottom panel as well.

Figure 7. Monthly mean of the wind stress curl during the six-month period. Contour interval is 0.1×10^{-7} $N\ m^{-3}$. Regions of negative curls are shaded.

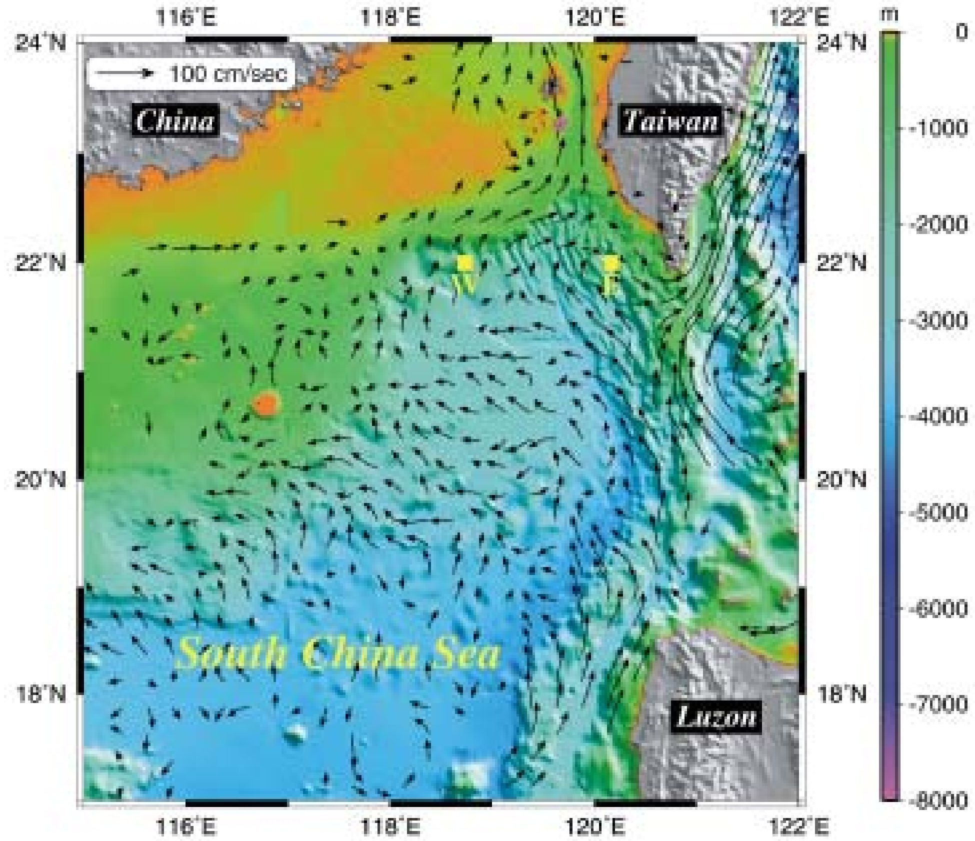

116°E
118°E
120°E
122°E
24°N
22°N
20°N
18°N
100 cm/sec
China
Taiwan
W
E
South China Sea
Luzon
m
0
-1000
-2000
-3000
-4000
-5000
-6000
-7000
-8000

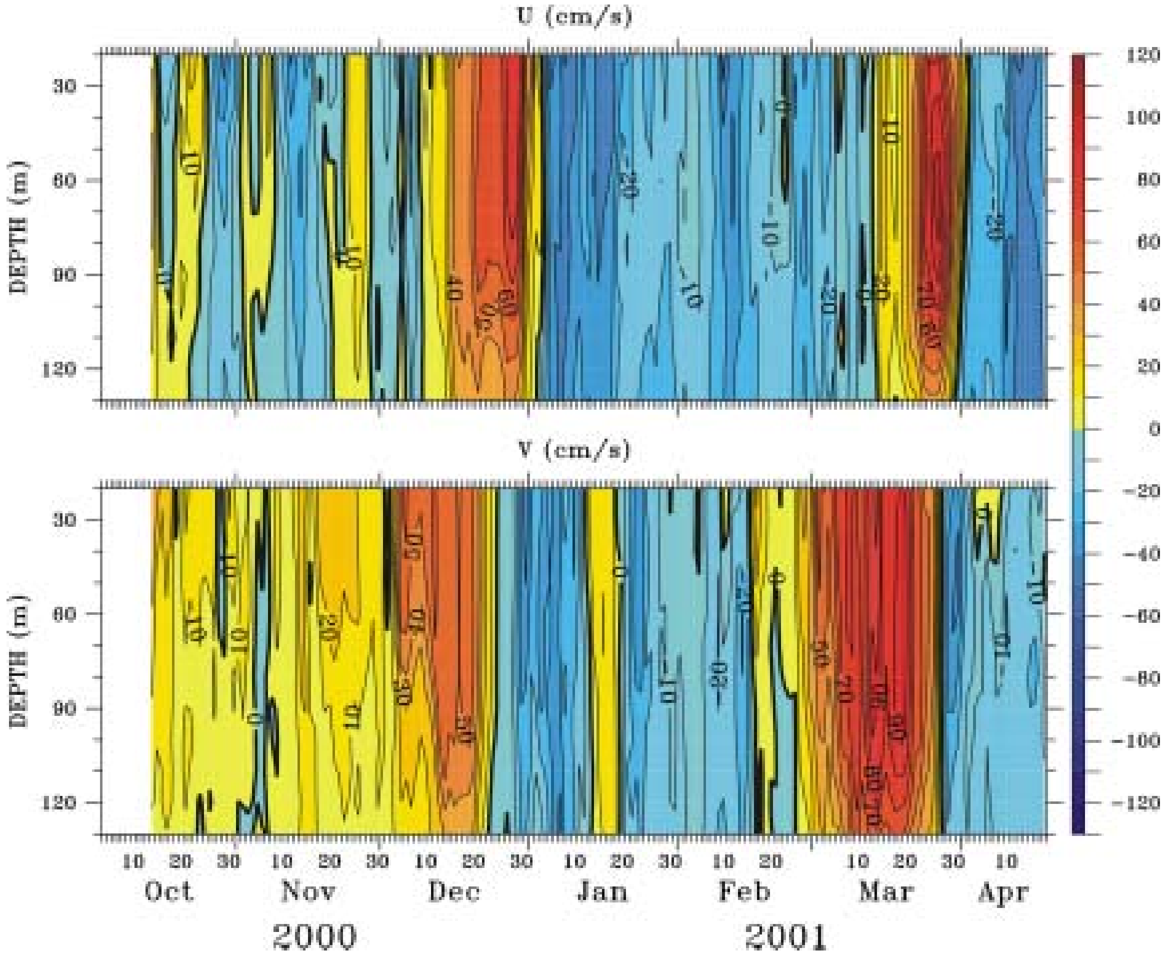

U (cm/s)
V (cm/s)
DEPTH (m)
30
60
90
120
120
100
80
60
40
20
0
-20
-40
-60
-80
-100
-120
10 20 30 10 20 30 10 20 30 10 20 30 10 20 10 20 30 10
Oct
Nov
Dec
Jan
Feb
Mar
Apr
2000
2001

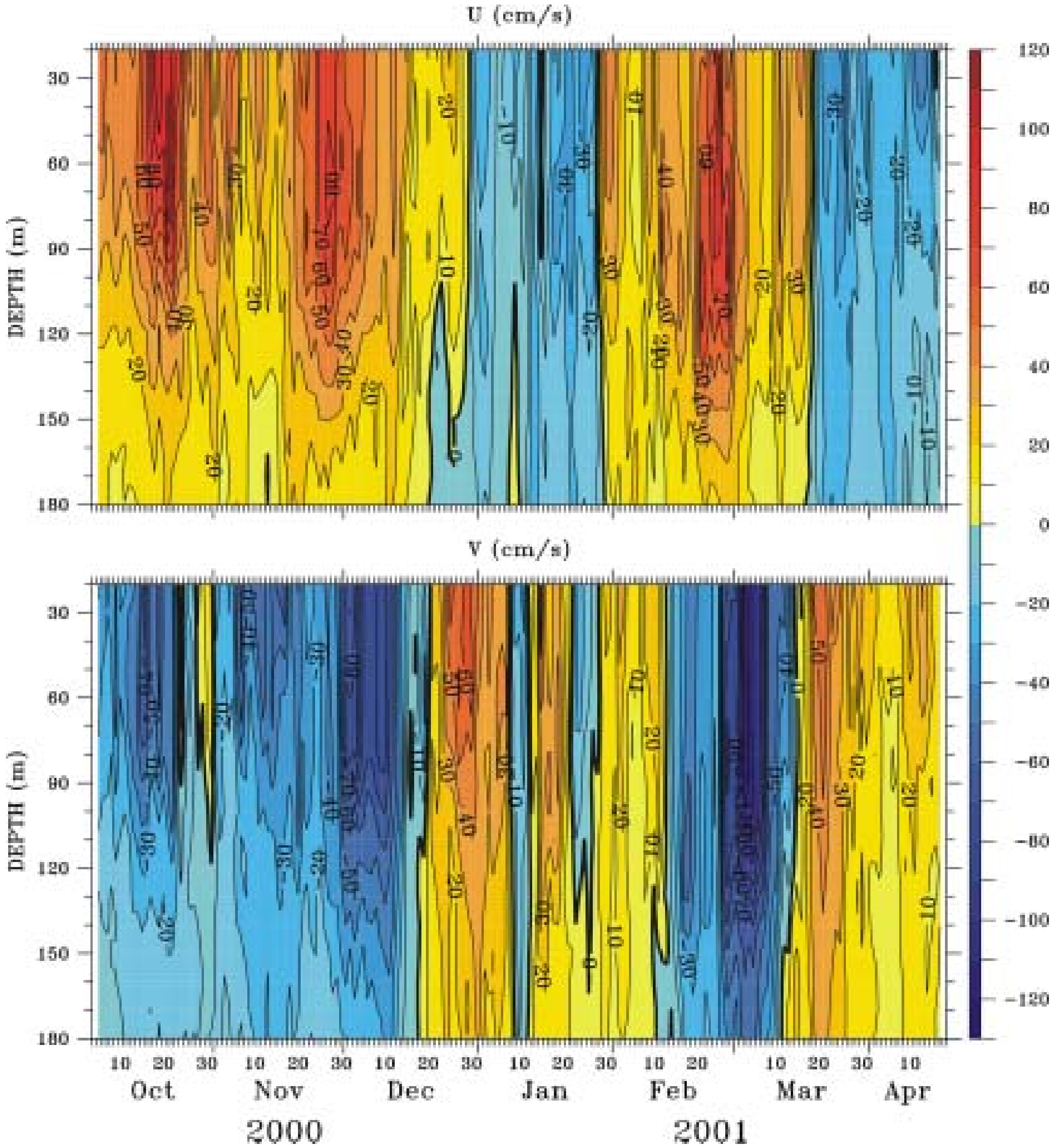
U (cm/s)
V (cm/s)
DEPTH (m)
Oct
Nov
Dec
Jan
Feb
Mar
Apr
2000
2001

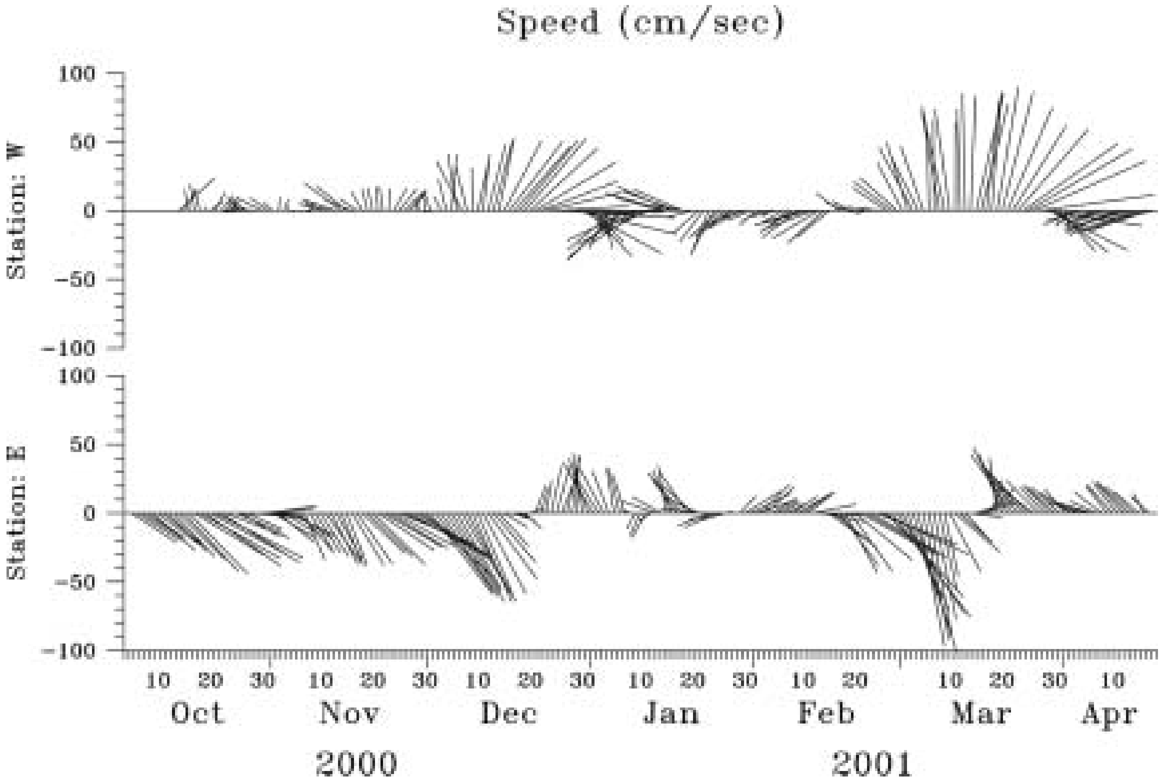
Speed (cm/sec)
Station: W
Station: E
100
50
0
-50
-100
10 20 30 10 20 30 10 20 30 10 20 30 10 20 10 20 30 10
Oct Nov Dec Jan Feb Mar Apr
2000
2001

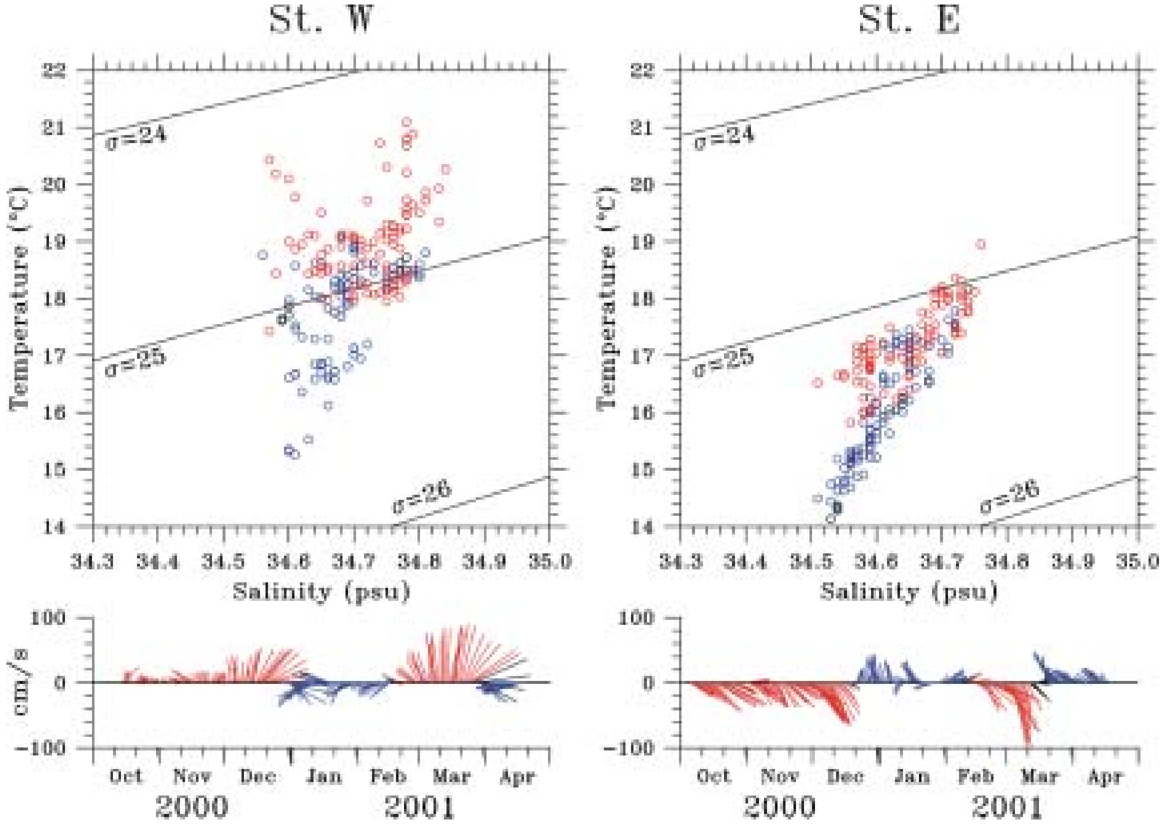

St. W
St. E
Temperature (°C)
Salinity (psu)
σ=24
σ=25
σ=26
cm/s
Oct
Nov
Dec
Jan
Feb
Mar
Apr
2000
2001

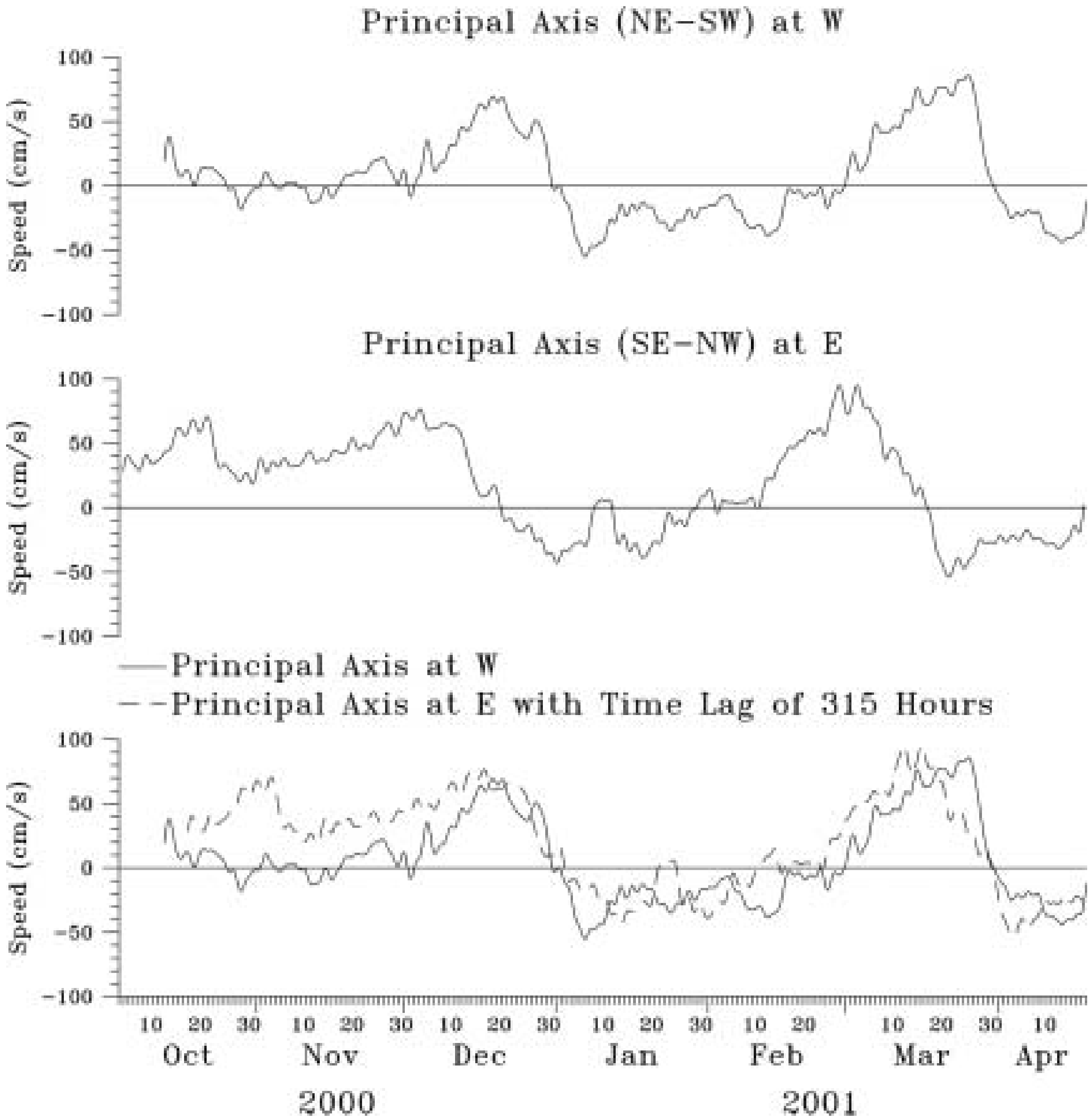

Principal Axis (NE−SW) at W
Speed (cm/s)
100
50
0
−50
−100
Principal Axis (SE−NW) at E
Speed (cm/s)
100
50
0
−50
−100
Principal Axis at W
Principal Axis at E with Time Lag of 315 Hours
Speed (cm/s)
100
50
0
−50
−100
10 20 30 10 20 30 10 20 30 10 20 30 10 20 10 20 30 10
Oct Nov Dec Jan Feb Mar Apr
2000
2001

Wind Stress Curl ($\times 10^{-7}$ N m^{-3})

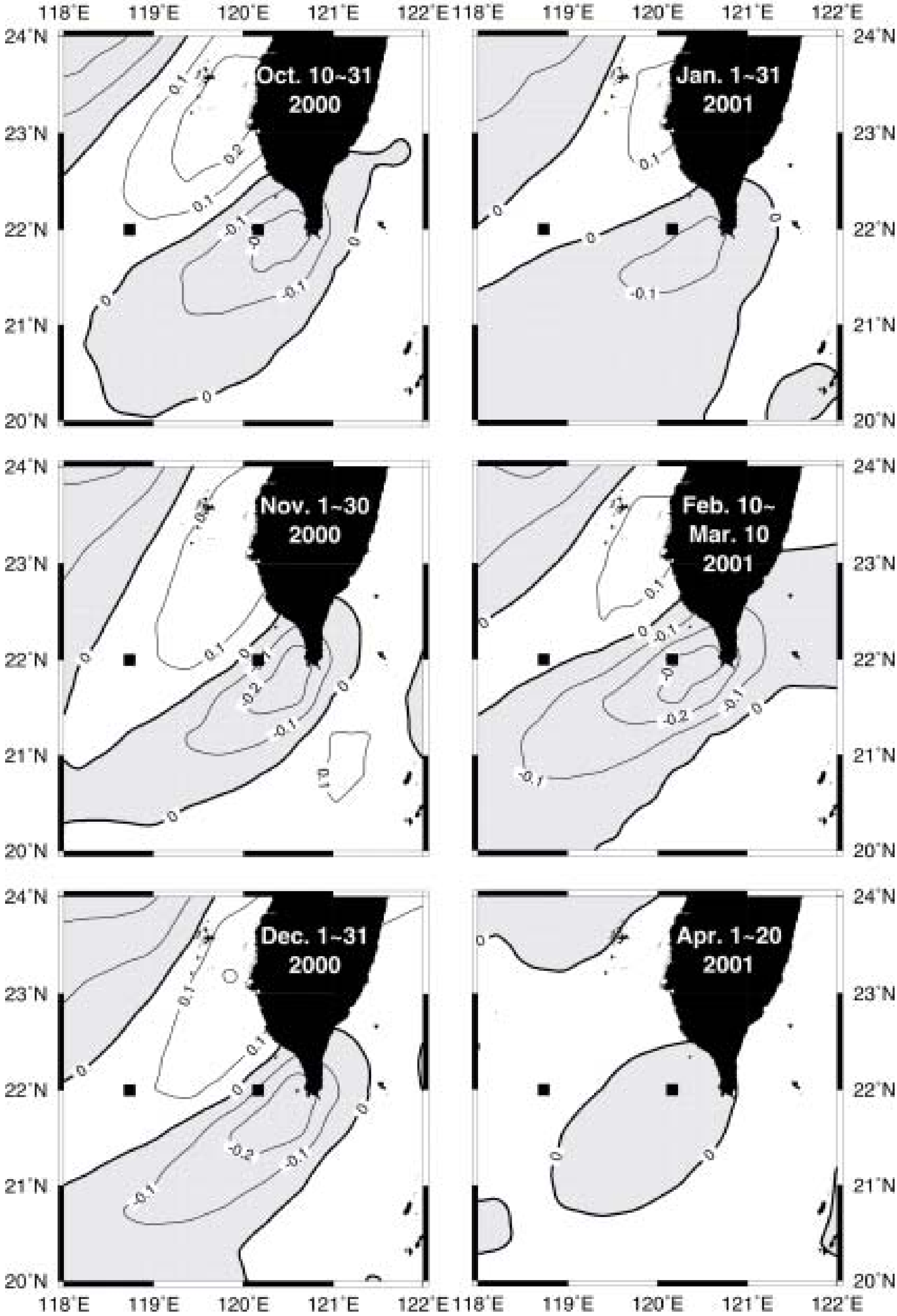

3. 討論

在“ Kuroshio Intrusion in Luzon Strait ”一文中, 使用的外力主要是歐洲中程氣象預報中心的表面風場, 其雖與實際量測風場在低頻部份相關性良好，唯其空間解析度為 2.5°x2.5°，無法適當地表現較高頻的變化, 所以文中我們成功地以數值模式 simulate 觀測結果的年及年際變化，但對 intra-seasonal 的 simulation 卻不太好，故現今我們仍以歐洲中程氣象預報中心的表面風場 spin-up 我們的模式，但將以衛星遙測風場來探對 intra-seasonal variation。為配合此我們亦將 refine 我們的模式, 期能成功地探討黑潮入侵呂宋海峽時的季節內變化的原因。

在“ Intra-seasonal variation in the velocity field of the northeastern South China Sea ”一文中，我們僅討論分析該處量測的海流變化，並推論其與 wind stress curl 之關係。進一步藉助數值模式模擬討論其變化動力機制的工作目前正在進行中。